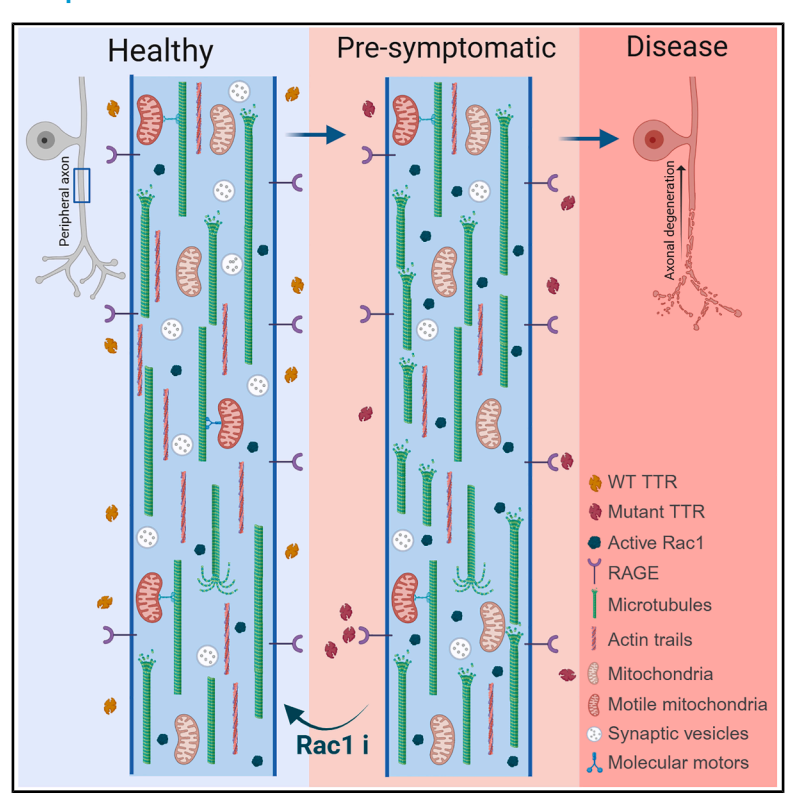
Cell Reports

Rac1 inhibition prevents axonal cytoskeleton dysfunction in transthyretin amyloid polyneuropathy

Graphical abstract



Authors

Joana Magalhães, Vítor Pacheco Dias, Jessica Eira, ..., Carolina Lemos, Sung-Tsang Hsieh, Márcia A. Liz

Correspondence

mrliz@icbas.up.pt

In brief

Magalhães et al. reveal that Rac1 hyperactivation disrupts axonal cytoskeleton and transport in a mouse model of transthyretin amyloid polyneuropathy. They show that Rac1 inhibition prevents axonal degeneration and identify a patient-associated RACGAP1 variant suggesting a neuroprotective role for Rac1 inactivation.

Highlights

- Actin and microtubule impairments precede axonal degeneration in a mouse model of ATTRv-PN
- Rac1 hyperactivation drives cytoskeleton disruption in ATTRv-PN
- Rac1 inhibition rescues cytoskeletal defects and prevents axonal degeneration
- A protective RACGAP1 variant, a Rac1 inactivator, delays disease onset in ATTRv-PN patients





Cell Reports



Article

Rac1 inhibition prevents axonal cytoskeleton dysfunction in transthyretin amyloid polyneuropathy

Joana Magalhães, ^{1,11} Vítor Pacheco Dias, ^{1,2,11} Jessica Eira, ^{1,11} Marina I. Oliveira da Silva, ¹ Guilherme Nóvoa, ¹ Margarida Martins, ¹ Yu Yu Kan, ³ Andreia Dias, ^{1,4} Estefânia Carvalho, ¹ Mariana Santos, ^{1,4,5} Ana I. Seixas, ¹ Teresa Coelho, ⁶ Ricardo Taipa, ^{4,5,7} Joana Paes-de-Faria, ¹ Carolina Lemos, ^{1,4,5} Sung-Tsang Hsieh, ^{8,9,12} and Márcia A. Liz^{1,4,5,10,12,13,*} ¹ IBMC -Instituto de Biologia Molecular e Celular and i3S - Instituto de Investigação e Inovação em Saúde, University of Porto, 4200-135 Porto,

Portugal ²Graduate Program in Molecular and Cell Biology, ICBAS - School of Medicine and Biomedical Sciences, University of Porto, 4050-313 Porto,

Portugal ³School of Medicine, College of Medicine, National Sun Yat-sen University, Kaohsiung 804201, Taiwan

⁴UMIB – Unit for Multidisciplinary Research in Biomedicine, ICBAS – School of Medicine and Biomedical Sciences, University of Porto, 4050-313 Porto, Portugal

⁵ITR - Laboratory for Integrative and Translational Research in Population Health, 4050-600 Porto, Portugal

⁶Unidade Corino de Andrade, Centro Hospitalar Universitário de Santo António, 4099-001 Porto, Portugal

⁷Department of Neuropathology, Centro Hospitalar Universitário de Santo António, 4099-001 Porto, Portugal

⁸Department of Anatomy and Cell Biology, National Taiwan University College of Medicine, Taipei 100233, Taiwan

⁹Department of Neurology, National Taiwan University Hospital, Taipei 100225, Taiwan

¹⁰Molecular Pathology and Immunology Department, ICBAS – School of Medicine and Biomedical Sciences, University of Porto, 4050-313 Porto, Portugal

¹¹These authors contributed equally

¹²Senior author

13Lead contact

*Correspondence: mrliz@icbas.up.pt https://doi.org/10.1016/j.celrep.2025.116411

SUMMARY

Hereditary transthyretin amyloidosis with polyneuropathy (ATTRv-PN) is characterized by the deposition of amyloidogenic transthyretin, particularly in dorsal root ganglia (DRG) and peripheral nerve axons, resulting in sensorimotor axonopathy. Here, we investigated cytoskeleton alterations in peripheral axons from an ATTRv-PN mouse model, the hTTRA97S knockin mice. Proteomics of hTTRA97S sural nerves revealed dysregulation of actin-related proteins. hTTRA97S DRG neurons presented a defective actin distribution in growth cones along with a reduction in axonal actin trails, impacting synaptic vesicle recycling. Microtubule dynamics and axonal transport abnormalities were also observed in mutant axons. Cytoskeletal defects in hTTRA97S neurons preceded axonal degeneration and were mediated by Rac1 hyperactivation. Importantly, Rac1 inhibition rescued cytoskeleton alterations, preventing degeneration. In late-onset ATTRv-PN patients, a variant in *RACGAP1*, encoding a Rac1 inactivator, supported the neuroprotective role of Rac1 inhibition. Our findings demonstrate that cytoskeletal defects precede axonopathy in ATTRv-PN and highlight Rac1 as a promising therapeutic target.

INTRODUCTION

Hereditary transthyretin amyloidosis with polyneuropathy (ATTRv-PN) is a fatal autosomal dominant neurodegenerative disease, characterized by the deposition of oligomers, aggregates, and amyloid fibrils of mutated transthyretin (TTR), particularly in the peripheral nervous system (PNS), leading to a distal axonopathy. Age of disease onset in ATTRv-PN presents great variability. Early-onset ATTRv cases (less than 50 years of age) are characterized by small-fiber-predominant axonal degeneration, leading to sensory dissociation, namely abnormal sensation symptoms, primarily due to amyloid fibril deposition around

nerve fibers. In contrast, late-onset cases (more than 50 years of age) involve both small and large fiber damage with loss of all sensory modalities, despite less amyloid deposition relative to the severity of nerve fiber loss. ^{2–4} These observations suggest the existence of mechanisms other than direct damage caused by amyloid fibers.

The available therapeutic options for ATTRv-PN comprise liver transplantation (the major organ of TTR synthesis), which slows disease progression in young-onset patients, ^{5,6} although it is highly invasive. Other therapies available include the use of TTR stabilizers and silencing *TTR* gene expression. ⁷⁻¹⁰ Besides the fact that the above therapies can only be applied after







disease onset, none of the available strategies targets the ongoing axonal degeneration. As such, the need to further characterize cellular and molecular pathways involved in ATTRv-PN-related axonopathy persists.

Abnormalities in cytoskeletal organization have been reported in several neurodegenerative disorders. 11 In the case of ATTRv-PN, the dying-back pattern of axonal degeneration suggests an initial disturbance of the distal cytoskeleton as a consequence of TTR deposition. Here, we explored the role of cytoskeletal dysregulation and Rac1 involvement in ATTRv-PN using a mouse model of the disease, the hTTRA97S mice. 12 These mice replicate the early degeneration of sensory nerves observed in ATTRv-PN. 12 The hTTRA97S mouse is a knockin model generated by replacing one allele of the mouse Ttr locus with human TTR bearing the A97S mutation (hTTRA97S) or, in the case of control mice, with human WT TTR (hTTRWT). 12 By approximately 24 months of age, the hTTRA97S mice present TTR deposition in peripheral nerves, decreased density of myelinated axons in the sural nerve (a purely sensory nerve), loss of intraepidermal nerve fibers in the skin, and mechanical allodynia. 12 Besides being a powerful model to test new therapeutic drugs, hTTRA97S mice are a valuable tool for dissecting the intracellular alterations occurring as a consequence of TTR deposition.

Our present findings reveal that Rac1-mediated cytoskeleton dysfunction, including disruption of the actin-vesicle network and defective microtubule dynamics and axonal transport, precedes axonal degeneration in ATTRv-PN. Notably, we demonstrate that Rac1 inhibition prevents degeneration of hTTRA97S peripheral axons. Importantly, we detected a genetic variant leading to the upregulated expression of the *RACGAP1* gene, which encodes the specific Rac1 inactivator Rac GTPase-activating protein 1 (RacGAP1),¹³ in late-onset patients, strongly suggesting that a decrease in Rac1 activity is neuroprotective. Collectively, we suggest Rac1 as a potential therapeutic target for ATTRv-PN.

RESULTS

Amyloidogenic TTR upregulates actin cytoskeleton molecular pathways in sensory axons

Characterizing the proteome profile of tissues affected by amyloidogenic TTR might elucidate the molecular mechanisms underlying ATTRv-PN pathogenesis. While previous studies have focused on tissues such as the liver, adipose tissue, and salivary glands from ATTR patients, 14,15 there are no available data on gene expression or profile of the disease in sensory neurons. To advance our understanding of axonal dysfunction in ATTRv-PN, we performed proteomic analysis of the sural nerve in 9-month-old hTTRA97S mice, a time point during which no axonal degeneration was observed, as evidenced by the unchanged density of myelinated axons in the sural nerve (Figures 1A and 1B) and the constant number of intraepidermal nerve fibers in the hind paw pad skin (Figures 1C and 1D). Moreover, we found that 9-month-old hTTRA97S mice displayed no defects in sensory performance, as determined by the von Frey test, in contrast to what we have observed in mice at 15 months of age (Figure 1E). These results confirm that 9 months is a pre-symptomatic stage of the disease, allowing us to characterize early proteomic alterations triggered by hTTRA97S. Additionally, both human and mouse TTR levels were comparable in hTTRA97S and hTTRWT sural nerves (Figures S1A–S1E).

Our proteomic analysis revealed 245 proteins that were differentially regulated in hTTRA97S nerves compared to hTTRWT controls (Table S1). Gene Ontology (GO) analysis of the 46 proteins with increased levels in mutant nerves revealed alterations in 4 molecular pathways, namely actin filament binding, calmodulin binding, actin binding, and cytoskeletal protein binding, with 8, 6, 9, and 11 dysregulated proteins in each GO term, respectively (Figures 1F and 1G). Given that some of the dysregulated proteins identified, such as TPM2 and SMTN, are also highly expressed in skeletal muscle, we performed a western blot for desmin, a muscle-specific intermediate filament protein, to assess potential contamination of our sural nerve samples. Desmin was nearly undetectable in all preparations, indicating minimal, if any, skeletal muscle contamination (Figures S1F and S1G).

In the case of downregulated proteins, the enrichment analysis exposed a scattered scenario, with 199 differentially expressed proteins revealing alterations in a wide range of molecular pathways. The top 5 overrepresented pathways were related to extracellular matrix binding, extracellular matrix structural constituent, structural constituent of ribosome, carboxylic ester hydrolase activity, and monocarboxylic acid binding (Figure S1H).

The significant enrichment of actin-binding proteins (Figure 1G) among the differentially regulated proteins in hTTRA97S sural nerves supported our hypothesis of axonal cytoskeleton abnormalities in ATTR-PN and prompted us to analyze actin organization in hTTRA97S neurons.

hTTRA97S sensory neurites have a defective F-actin network preceding axonal degeneration

To uncover actin cytoskeleton defects in the ATTRv-PN mouse model, we resorted to DRG neuron cultures to analyze sensory neurites in the technical impossibility of investigating actin dynamics in sural nerve axons. We initially assessed the molecular relevance of our proteomic findings in the cellular system, focusing on actin-binding proteins. In hTTRA97S sural nerves, we identified increased levels of Arpc1a, a subunit of the Arp2/3 complex involved in actin filament branching (Figure 1G). To confirm the molecular relevance of this finding in DRG neurons, we examined Arp2/3 complex expression in DRG-derived axons. Due to technical limitations in detecting Arpc1a, we assessed ARP3, a core subunit of the same complex, by western blot. This analysis revealed increased ARP3 protein levels in hTTRA97S DRG cultures compared to controls (Figures S2A and S2B), thereby recapitulating the proteomic data obtained from the sural nerve.

We followed by analyzing whether hTTRA97S DRG neurites presented actin cytoskeleton alterations at the growth cone, similarly to what we have observed in photoreceptor axons from ATTRv-PN flies. Although only present in growing neurons, the growth cone is a suitable cellular structure to study neuronal cytoskeleton rearrangements, as both microtubules and actin are stereotypically organized within this neuronal component. We categorized growth cone morphology using phalloidin staining into two different types as previously reported 17: fan-shaped growth cone, characterized by an



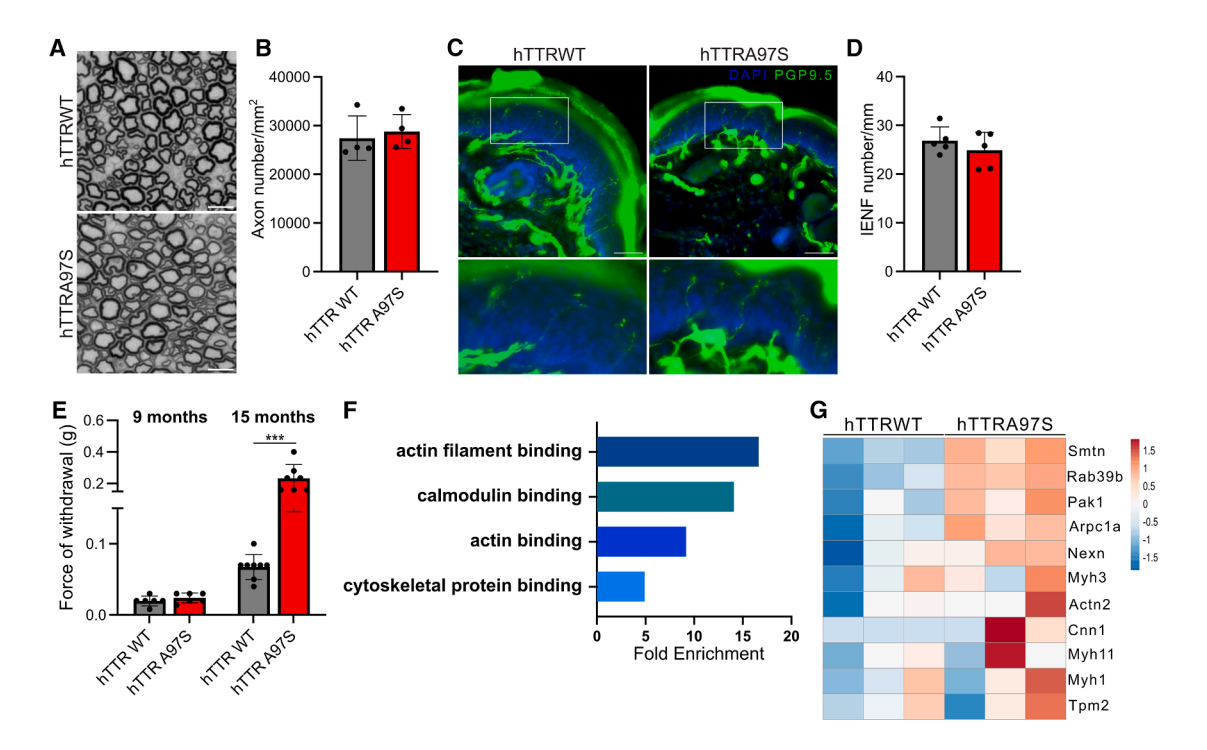


Figure 1. Amyloidogenic TTR upregulates actin cytoskeleton molecular pathways in sensory axons before disease onset

(A and B) Representative images of toluidine blue-stained semi-thin sections of hTTRWT and hTTRA97S sural nerves at 9 months of age (A) and corresponding density of myelinated axons (B). Scale bar, $5 \mu m$. Data represent mean \pm SD of n = 4 animals per genotype.

- (C) Representative images of footpad sections from hTTRWT and hTTRA97S mice immunostained for protein gene product 9.5 (green); DAPI (blue). Scale bar, 50 um.
- (D) Quantification of intraepidermal nerve fiber (IENF) density relative to (C). Results presented as mean \pm SD of n=5 animals per genotype.
- (E) von Frey test in 9- and 15-month-old hTTRWT and hTTRA97S mice. Data represent mean \pm SD of n = 6-8 animals per genotype.
- (F) Fold enrichment of Gene Ontology categories for molecular function of upregulated proteins in hTTRA97S sural nerves. Gene Ontology analyses were performed using PANTHER 19.0.
- (G) Heatmap of actin-related proteins differentially expressed between 9-month-old hTTRWT and hTTRA97S mice.
- ***p < 0.001 by Student's t test.

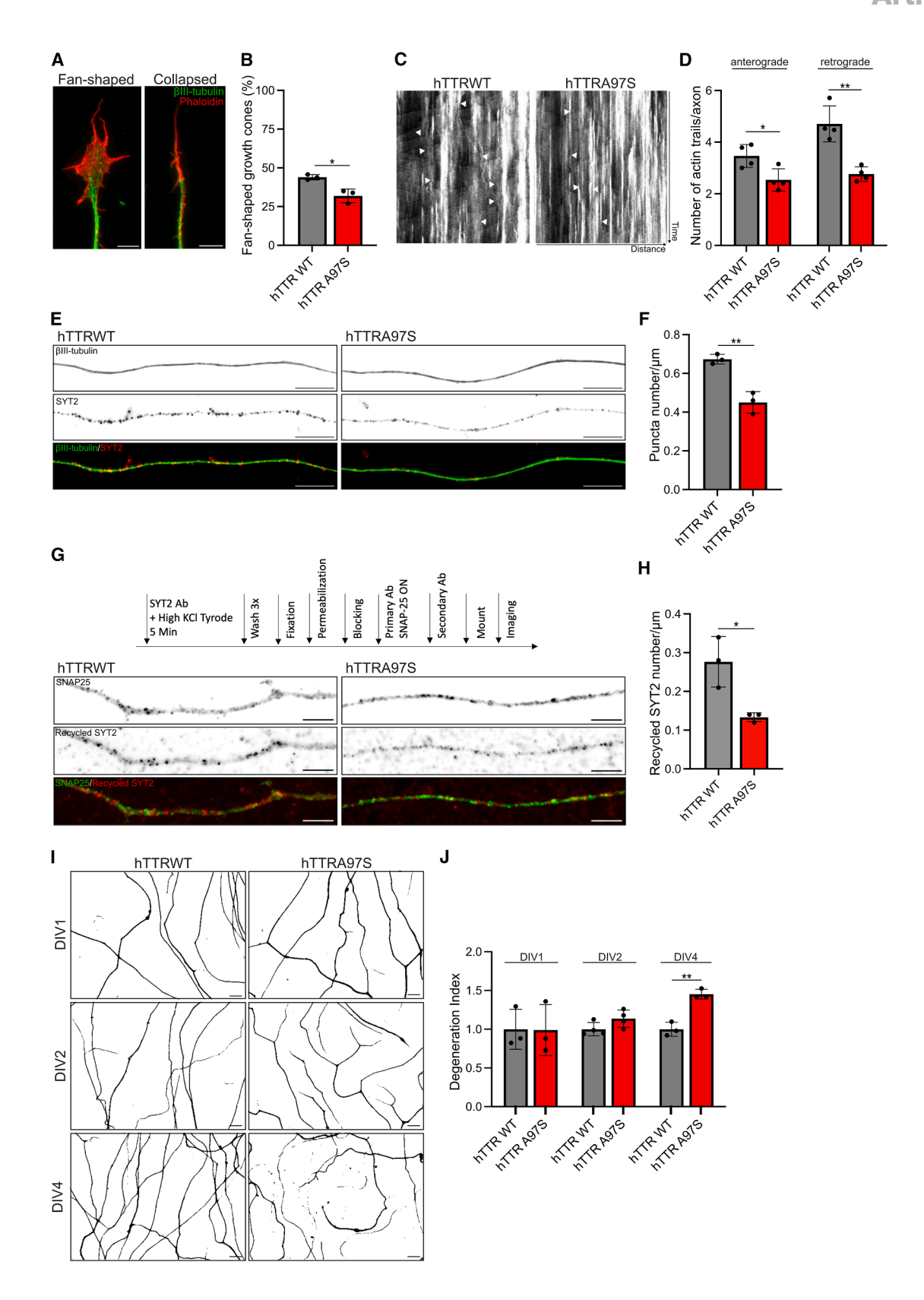
See also Figure S1.

expanding cone larger than its proximal area, containing the typical lamellipodia and filopodia structures (Figure 2A, left); and collapsed growth cone, characterized by a thin shaped cone lacking the lamellipodial/filopodial organization (Figure 2A, right). We initially performed DRG neuron cultures from 9-monthold mice, matching the age used for in vivo analyses. However, similar results were obtained from cultures prepared at 1, 3, 6, and 9 months of age (Figure S2C). At DIV1, approximately 45% of hTTRWT DRG neurons displayed fan-shaped growth cones, consistent with previous observations in adult WT neurons. 18 In contrast, hTTRA97S neurons showed consistent ~27% reduction in fan-shaped growth cones through all ages analyzed (Figures 2B and S2C), indicating a stable growth cone collapse phenotype. To further assess whether this phenotype was common across DRG subtypes, we performed immunostaining for TrkA, TrkB, and TrkC in cultured DRG neurons and analyzed growth cone morphology within each subtype. hTTRA97S neurons exhibited a similar decrease in fan-shaped growth cones across all three populations, indicating that actin dysregulation occurs broadly among DRG subtypes (Figure S2D). While most growth cone analyses were

performed using DRGs from all spinal levels to maximize yield, we also confirmed similar results using only L3-L5 DRGs, aligning with the sural nerve data (Figure S2E).

Considering the axonopathy phenotype of ATTRv-PN, we analyzed axonal actin organization in DIV2 hTTRA97S DRG neurons. We tracked actin dysregulation in DRG axons by evaluating actin trails, which are fast linear events of F-actin polymerization that travel throughout the axon. 19 To measure axonal actin trails dynamics, we performed live imaging of DRG neurons transfected with a reporter expressing GFP fused to the calponin homology domain of utrophin (GFP:UTR-CH), which binds specifically to F-actin without significantly affecting its dynamics.²⁰ The nature of the actin trails displayed by control hTTRWT DRG neurons shared parameters with those previously reported in hippocampal neurons, 19 such as the rate of polymerization, although the length of the trails was slightly reduced (Table S2). Additionally, latrunculin, an F-actin depolymerizer previously shown to reduce the frequency of actin trails in hippocampal neurons, 19 had a similar effect on control DRG neurons (Figures S2F and S2G). We then analyzed axonal actin trail trafficking in hTTRWT and hTTRA97S DRG neurites. While







we did not find any differences regarding the length or rate of F-actin polymerization comparing the two genotypes (Figures S2H and S2I), we observed a reduction in the number of actin trails running both retrogradely and anterogradely in hTTRA97S DRG axons, supporting an axonal actin dysfunction (Figures 2C and 2D).

The transport of F-actin along axons, facilitated by actin trails, was shown to support the presynaptic enrichment of F-actin, a critical process for synaptic physiology. 19 Additionally, axonal actin dynamics was related to the motion and recruitment of synaptic vesicles by regulating synaptic vesicle recycling. 19,21 To assess whether a reduction in the number of actin trails could affect synaptic vesicles in hTTRA97S axons, we immunolabelled DRG neurons with synaptotagmin-2, a protein embedded in the membrane of synaptic vesicles, which functions as a calcium sensor that triggers the vesicle's fusion with the presynaptic membrane. In fixed cells, we observed a reduction in the levels of synaptotagmin-2 in hTTRA97S neurons (Figures 2E and 2F). To determine whether the reduction in synaptotagmin-2 signal observed in fixed hTTRA97S neurons reflects a functional impairment in synaptic vesicle cycling, we performed a live-cell antibody uptake assay using an antibody that recognizes a luminal epitope of synaptotagmin-2. This epitope becomes transiently exposed to the extracellular medium upon synaptic vesicle fusion with the plasma membrane and is internalized during endocytosis, thereby allowing selective labeling of actively recycling vesicles. DRG neurons were stimulated with high KCl in the presence of the synaptotagmin-2 antibody and subsequently fixed. After immunostaining for SNAP-25 to define synaptic regions, a significant reduction in synaptotagmin-2 uptake in hTTRA97S neurons was observed when compared to controls (Figures 2G and 2H). These findings indicate a defect in synaptic vesicle recycling.

We followed by assessing whether the actin alterations mediated by hTTRA97S were related to axonal damage by measuring axonal degeneration in hTTRWT and hTTRA97S DRG neurons. Axonal degeneration, as determined by degeneration index measurements, ²² was not different between hTTRA97S and

hTTRWT neurons at DIV1, the time point of growth cone morphology analysis, or at DIV2, when axonal actin defects were observed (Figures 2I and 2J). However, by DIV4, hTTRA97S DRG neurons exhibited axonal fragmentation, as shown by an increased degeneration index compared to hTTRWT neurons (Figures 2I and 2J). These results demonstrate that defects in actin organization and dynamics, along with a concomitant impact on axonal synaptic vesicle recycling, precede axonal degeneration of hTTRA97S DRG neurons.

Microtubule dynamics and axonal transport are impaired in hTTRA97S axons, reflecting a generalized cytoskeleton dysfunction

Considering the crosstalk between actin and microtubules and the emerging recognition of alterations in microtubule stability and axonal transport as common features of dying-back axonopathies,²³ we sought to investigate additional cytoskeleton alterations in hTTRA97S mice. Leveraging transgenic mice expressing the microtubule plus-end binding protein EB3 fused to green fluorescent protein (GFP) under the control of the neuron-specific Thy1 promoter (Thy1:EB3-GFP),²⁴ we examined microtubule dynamics in the sural nerve of hTTRA97S mice. We generated hTTRA97S-Thy1-EB3-GFP and hTTRWT-Thy1-EB3-GFP mice and performed ex vivo live imaging of sural nerves from pre-symptomatic 9-month-old animals, an age preceding axonal degeneration. Our data revealed an increase in EB3 comet density with no alterations in growth rate, in hTTRA97S-Thy1-EB3-GFP mice when compared to control hTTRWT-Thy1-EB3-GFP animals (Figures 3A-3C). The observed increase in EB3 comet density, combined with the lack of differences in total microtubule density assessed by electron microscopy of cross sections of hTTRWT and hTTRA97S sural nerves (Figures S3A and S3B), suggests an increase in dynamic microtubule plus-ends in hTTRA97S axons.

In the axonal shaft, a tight balance between microtubule stability and dynamics is critical to enable normal axon physiology. The increased microtubule dynamics in the shaft of hTTRA97S axons could therefore underlie the dysregulation of such crucial

Figure 2. Alterations in the actin-vesicle network of hTTRA97S DRG neurons precede axonal degeneration

(A and B) Representative images of fan-shaped and collapsed growth cones of DRG neurons double-labeled with β III-tubulin antibody (green) and phalloidin (red) (A) and respective quantification of the proportion of fan-shaped ones in DIV1 hTTRWT and hTTRA97S neurons (B). Scale bar, 5 μ m. Data represent mean \pm SD of n=3 independent experiments, each performed on independent neuronal cultures from WT and A97S genotypes (approximately 100 growth cones analyzed per genotype in each experiment).

(C and D) Representative kymographs of imaged axons transfected with GFP:UTR-CH (to label F-actin) (C) and respective quantification of the number of retrograde and anterograde actin trails in DIV2 hTTRWT and hTTRA97S neurons (D). White arrowheads mark vectorial plumes of fluorescence (actin trails). Data represent mean \pm SD of n=4 independent experiments, each performed on independent neuronal cultures from WT and A97S genotypes (12–20 axons analyzed per genotype in each experiment).

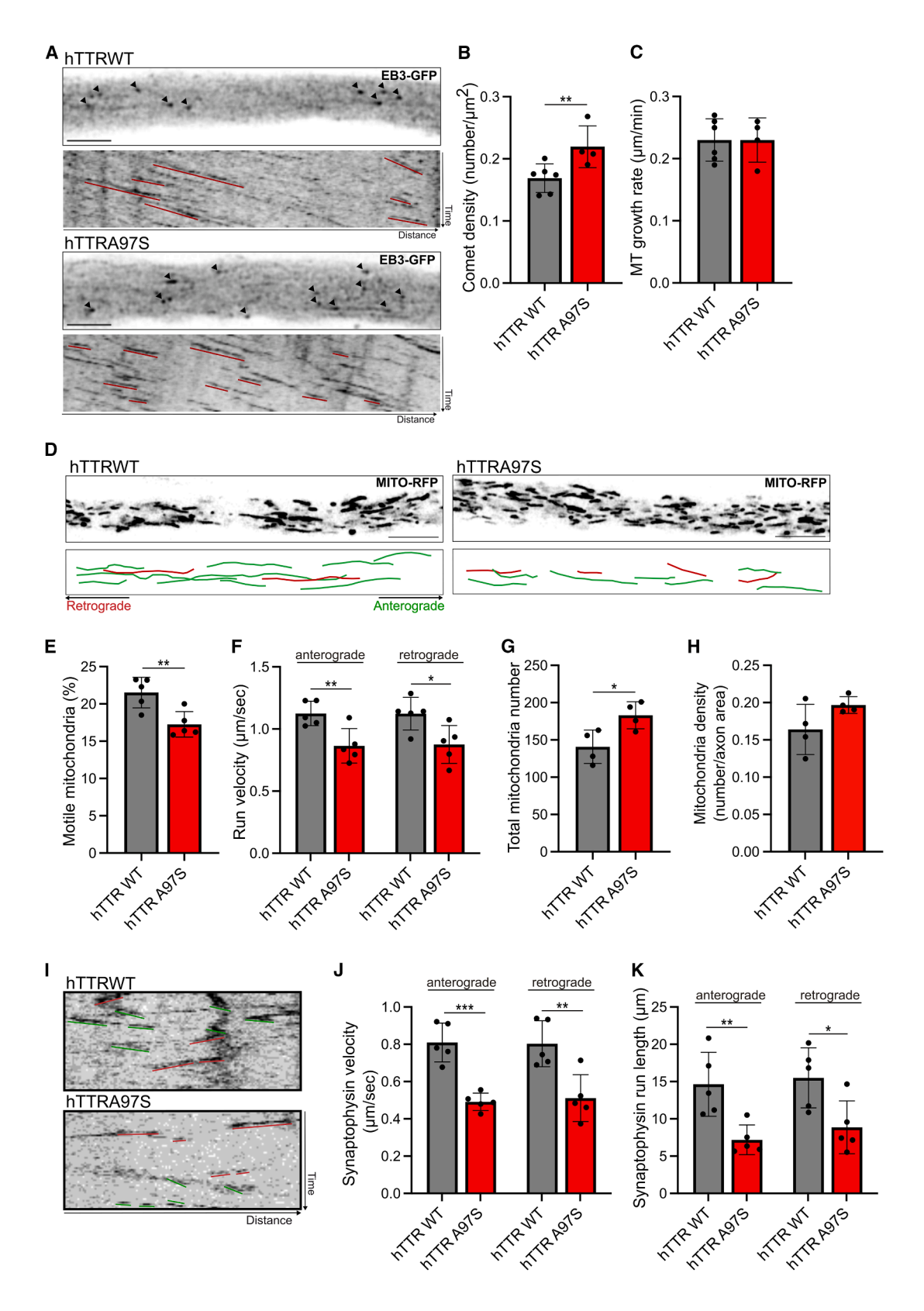
(E and F) Representative images of DIV2 hTTRA97S and hTTRWT DRG axons double-labeled with β III-tubulin (green) and synaptotagmin-2 (SYT2, red) (E) and respective quantification of the number of synaptotagmin puncta per axon length (F). Scale bar, 10 μ m. Data represent mean \pm SD of n=3 independent experiments, each performed on independent neuronal cultures from WT and A97S genotypes (17–30 axons analyzed per genotype in each experiment).

(G) Schematic outline of the experimental set up and representative images of synaptotagmin-2 (SYT2) antibody uptake (red) from DIV2 hTTRA97S and hTTRWT DRG neurons, immunolabeled for the presynaptic marker SNAP-25 (green). Scale bar, 5 µm.

(H) Quantification of the number of recycling synaptotagmin vesicles, colocalized with SNAP-25, per axon length relative to (G). Data represent mean \pm SD of n=3 independent experiments, each performed on independent neuronal cultures from WT and A97S genotypes (15–20 axons analyzed per genotype in each experiment).

(I and J) Representative immunofluorescence images of β IIII-tubulin stained DIV1, DIV2, and DIV4 hTTRWT and hTTRA97S DRG neurons (I) and respective quantification of degeneration index (J). Scale bar, 10 μ m. Data represent mean \pm SD of n=3 independent experiments, each performed on independent neuronal cultures from WT and A97S genotypes (20–25 images analyzed per genotype in each experiment). $^*p < 0.05$, $^*p < 0.01$ by Student's t test. See also Figure S2.





(legend on next page)



balance and potentially lead to axon pathology, particularly to defective axonal transport. To explore this further, we analyzed the transport of mitochondria by crossing hTTRA97S or hTTRWT mice with Thy1-Mito-RFP mice, which express a mitochondrial sequence fused to RFP under the neuronal Thy1 promoter,²⁵ thereby generating hTTRA97S-Thy1-Mito-RFP and hTTRWT-Thy1-Mito-RFP mice. Through ex vivo live imaging of sural nerves from 9-month-old animals, we observed a reduction in the percentage of motile mitochondria in hTTRA97S-Thy1-Mito-RFP nerves compared to the control group (Figures 3D and 3E). Also, the motile mitochondria in the mutant axons exhibited reduced anterograde and retrograde velocities, as well as shorter run lengths in both directions (Figures 3F and S3C). To address whether the observed impaired trafficking of mitochondria was related to alterations in mitochondrial abundance, we quantified the total number of mitochondria and observed an increase in hTTRA97S sural nerve axons compared to controls (Figure 3G). While there was also a trend toward increased mitochondrial density (total number of mitochondria normalized to axonal area), this did not reach statistical significance (Figure 3H). Nevertheless, the increased number of mitochondria may reflect compensatory or pathological accumulation in mutant axons, and the reduced motility likely results from disrupted trafficking machinery or crowding effects along the axon, both potentially downstream of cytoskeletal alterations triggered by mutant TTR.

To address additional axonal transport alterations, we analyzed synaptophysin transport by transducing DRG neurons with lentivirus expressing synaptophysin-GFP, which transduced hTTRWT and hTTRA97S DRG neurons with similar efficiency (Figures S3D and S3E). In hTTRA97S neurons, we observed a reduction in synaptophysin vesicle transport velocity, affecting both anterograde and retrograde directions, accompanied by a significant decrease in vesicle run length (Figures 3I–3K).

Together, our results suggest that hTTRA97S induces dysfunctions in both actin and microtubule cytoskeleton within peripheral axons, leading to impaired axonal transport. Importantly, these phenotypes precede axonopathy, suggesting that targeting cytoskeleton damage by modulating the underlying molecular mechanisms in ATTRv-PN could potentially prevent neurodegeneration.

Rac1 hyperactivation leads to cytoskeleton defects in hTTRA97S axons

In a previously reported genetic screen using an ATTR-PN model in which the amyloidogenic mutant TTRV30M was expressed in

photoreceptor cells, we demonstrated that reducing levels of Rac1 and Cdc42, members of the Rho GTPase family, ameliorated the TTR-induced rough eye phenotype. 16 Additionally, Rac1 silencing rescued the photoreceptors' axonal growth defects in TTRV30M expressing larvae. 16 Building on this, we analyzed the involvement of Rac1 in hTTRA97S axonal cytoskeleton alterations. Using live cell imaging with a FRET-based Rac1 biosensor,²⁶ we detected Rac1 hyperactivation in DRG neurite shafts from hTTRA97S mice, evidenced by a 45% increase in the FRET/CFP ratio of the Rac1 FRET probe compared to hTTRWT control neurons (Figures 4A and 4B). To further assess Rac1 activity, we performed pull-down assays on sciatic nerves from hTTRA97S mice. We used sciatic nerve lysates for the Rac1 pull-down assay due to the higher protein yield compared to sural nerve. Although mixed, the sciatic nerve is predominantly sensory (~71% sensory axons),²⁷ making it appropriate for studying sensory-related mechanisms. We observed an increase in Rac1 activity in hTTRA97S sciatic nerves from 9-month-old mice (Figures 4C and 4D), as demonstrated by an increase in Rac1-GTP levels with no alteration in total Rac1 levels. These results demonstrate that the presence of mutant TTR in peripheral nerves results in an increase in Rac1 activity at an age preceding disease symptomatology.

Given the increased Rac1 activity in hTTRA97S mice and the critical role of the Rho GTPase in cytoskeleton regulation, we next examined whether Rac1 mediates actin damage in mutant neurons. We found that either silencing (Figures S4A-S4C) or blocking Rac1 activity using the Rac1 inhibitor NSC23766 (Figure 4E) reverted actin cytoskeleton alterations in the growth cone of hTTRA97S neurons. To investigate the mechanism underlying Rac1 modulation in hTTRA97S neurons, we hypothesized that amyloidogenic TTR may activate Rac1 through its interaction with the receptor for advanced glycation end products (RAGEs). RAGE has been shown to bind amyloidogenic TTR, mediating its intracellular effects,²⁸ and also to activate Rho GTPases, including Rac1, in other cellular contexts.²⁹ These findings suggest that TTR-RAGE engagement could lead to Rac1 hyperactivation. To test this hypothesis, we treated hTTRA97S DRG neurons with the RAGE-specific antagonist FPS-ZM1³⁰ and observed a rescue of the growth cone collapse phenotype, similar to the one seen with Rac1 inhibition (Figure S4D). Moreover, combined treatment with both the RAGE antagonist and the Rac1 inhibitor did not yield an additive effect, indicating that they likely act through a shared pathway (Figure S4D). Altogether, these results support a model in which amyloidogenic TTR activates Rac1 via RAGE, contributing to actin cytoskeleton dysregulation.

Figure 3. Ex vivo live imaging of hTTRA97S sural nerve axons reveals alterations in microtubule dynamicity and transport of mitochondria (A–C) Representative EB3-GFP still images of the axonal shaft from hTTRWT-Thy1-EB3-GFP and hTTRA97S-Thy1-EB3-GFP sural nerves with corresponding kymographs (A), and respective quantifications of EB3 comet density (B) and microtubule growth rate (C). Scale bar, 5μ m. Data represent mean \pm SD of n = 4-6 animals per genotype (5–6 axons analyzed per animal).

(D–H) Representative still images of Mito-RFP in hTTRWT-Thy1-Mito-RFP and hTTRA97S-Thy1-Mito-RFP sural nerve axons (D) and respective quantification of the percentage of motile mitochondria (E), mitochondrial run velocity (F), total number of mitochondria (G), and mitochondria density (total number of mitochondria normalized by axon area) (H). Scale bar, 10 μ m. Data represent mean \pm SD of n = 4-5 animals per genotype (5 axons analyzed per animal).

(I–K) Representative kymographs of imaged neurites from DIV2 hTTRWT and hTTRA97S DRG neurons expressing synaptophysin-GFP (I) and respective quantification of synaptophysin velocity (J) and run length (K). Data represent mean \pm SD of n=5 independent experiments, each performed on independent neuronal cultures for WT and A97S genotypes (3–11 axons analyzed per genotype in each experiment).

*p < 0.05, **p < 0.01, ***p < 0.01 by Student's t test. See also Figure S3.



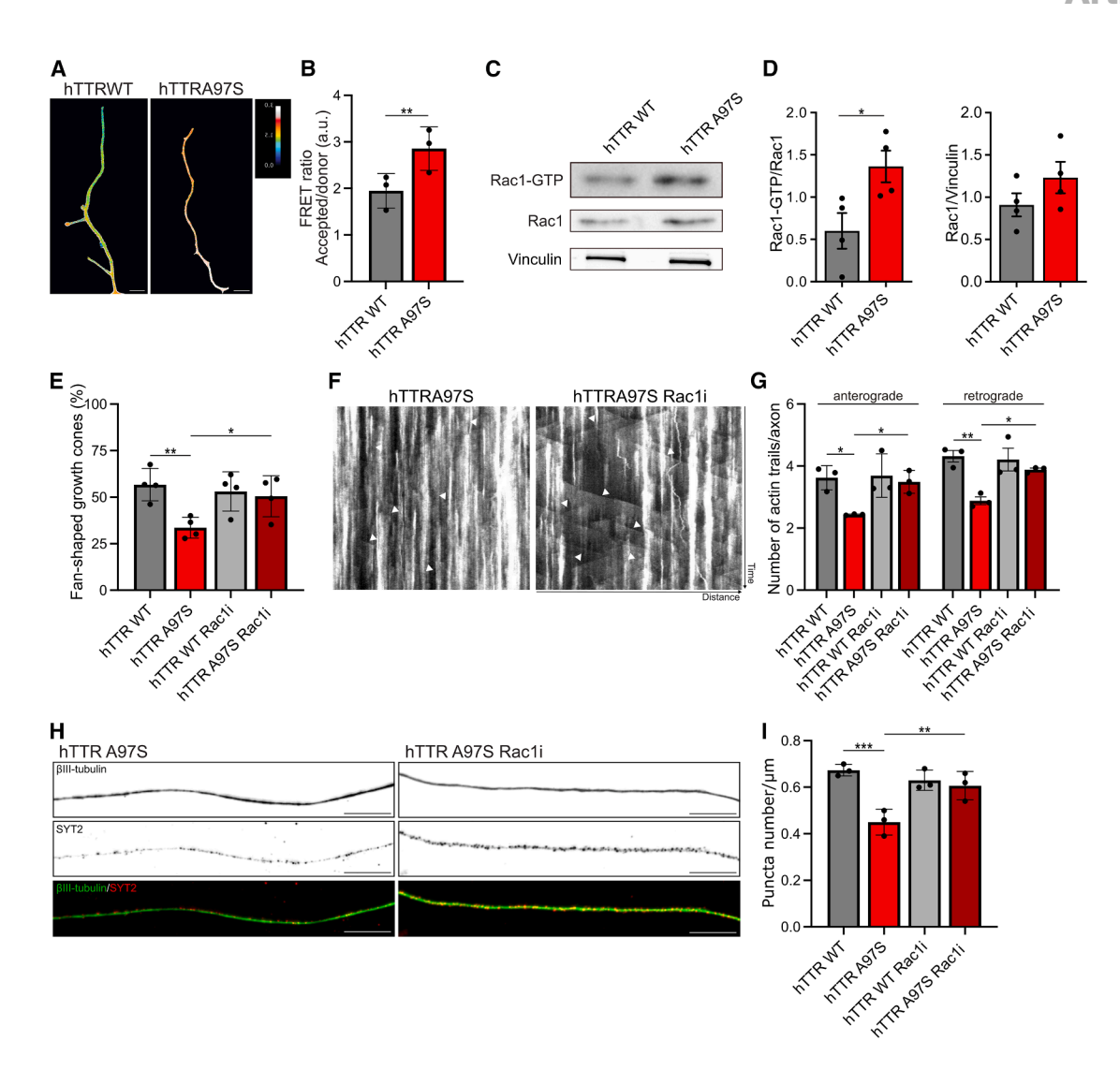


Figure 4. Rac1 activity is increased in hTTRA97S axons and its inhibition prevents actin-vesicle defects

(A and B) Pseudocolored images displaying the pixel value of the FRET ratio in neurites from DIV2 hTTRWT and hTTRA97S DRG neurons transfected with Raichu-Rac1 biosensor (A), and respective quantification (B). Scale bar, $10 \mu m$. Data represent mean \pm SD of n = 3 independent experiments, each performed on independent neuronal cultures for WT and A97S genotypes (20 axons analyzed per genotype in each experiment).

(C and D) Representative western blot analysis (C) and quantification (D) of Rac1 GTP-bound (active) levels by pull-down assay of 9-month-old hTTRWT and hTTRA97S sciatic nerves. The activated fraction was calculated by normalizing signal densities of GTP-bound to total Rac1 GTPase. Total levels of Rac1 are relative to vinculin. Data represent mean \pm SD of n = 4 animals per genotype.

- (E) Quantification of the percentage of fan-shaped growth cones in DIV1 hTTRWT and hTTRA97S neurons untreated or treated with 50 μM Rac1 inhibitor NSC23766 (Rac1i). Data represent mean ± SD of *n* = 4 independent experiments, each performed on independent neuronal cultures for WT and A97S genotypes (approximately 100 growth cones analyzed per condition in each experiment).
- (F) Representative kymographs of imaged axons transfected with GFP:UTR-CH (to label F-actin) from DIV2 hTTRA97S DRG neurons untreated or treated with 50 μM Rac1 inhibitor NSC23766 (Rac1i).
- (G) Quantification of the number of retrograde and anterograde actin trails in DIV2 hTTRWT or hTTRA97S neurons untreated or treated with 50 μ M Rac1 inhibitor NSC23766. Data represent mean \pm SD of n=3 independent experiments, each performed on independent neuronal cultures for WT and A97S genotypes (15–20 axons analyzed per condition in each experiment).
- (H) Representative images of axons from DIV2 hTTRA97S DRG neurons, untreated or treated with 50 μ M Rac1 inhibitor NSC23766 (Rac1i), double-labeled with β III-tubulin (green) and synaptotagmin-2 (SYT2, red). Scale bar, 10 μ m.
- (l) Quantification of the number of synaptotagmin puncta per axon length in DIV2 hTTRWT or hTTRA97S neurons untreated or treated with 50 μ M Rac1 inhibitor NSC23766. The quantification shown for WT and hTTRA97S conditions corresponds to the same dataset presented in Figure 2E (control conditions), as these were derived from the same set of experiments. Data represent mean \pm SD of n=3 independent experiments, each performed on independent neuronal cultures for WT and A97S genotypes (17–30 axons analyzed per condition in each experiment).
- *p < 0.05, **p < 0.01 by Student's t test (B and D). *p < 0.05, **p < 0.01, ***p < 0.001 by one-way ANOVA with Sidak's multiple comparisons test (E, G, and I). See also Figure S4.



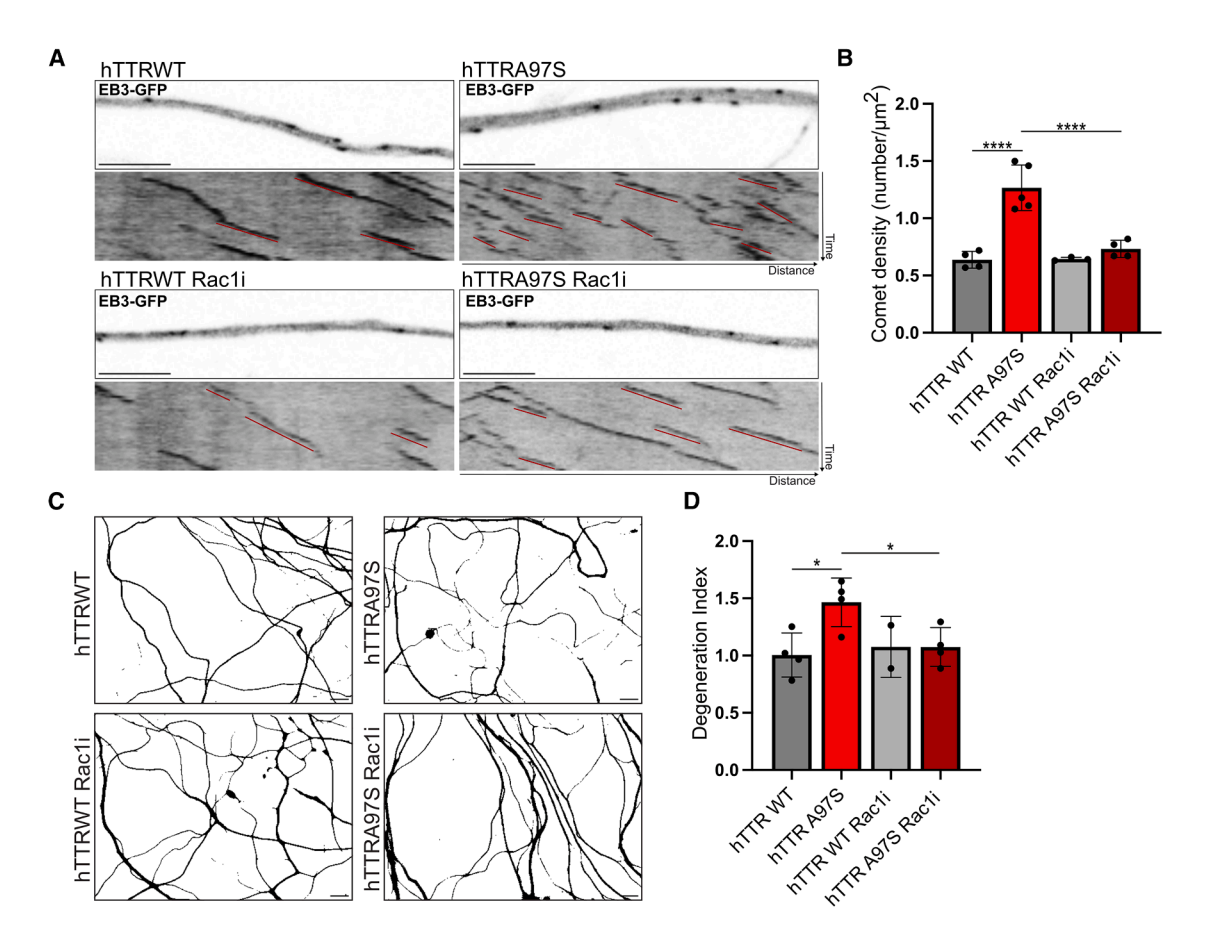


Figure 5. Rac1 inhibition reverts microtubule alterations and axonal degeneration in hTTRA97S neurons

(A and B) Representative EB3-GFP still images of the axonal shafts from DIV2 hTTRWT-Thy1-EB3-GFP or hTTRA97S-Thy1-EB3-GFP DRG neurons, untreated or treated with 50 μ M Rac1 inhibitor NSC23766 (Rac1i) (A), and corresponding quantification of EB3 comet density (B). Scale bar, 5 μ m. Data represent mean \pm SD of n = 3-5 independent experiments, each performed on independent neuronal cultures for WT and/or A97S genotypes (6–14 axons analyzed per condition in each experiment).

(C and D) Representative immunofluorescence images of β III-tubulin stained DIV4 hTTRWT and hTTRA97S DRG untreated or treated with 50 μ M Rac1 inhibitor NSC23766 (Rac1i) (C), and respective quantification of the degeneration index (D). Scale bar, 10 μ m. Data represent mean \pm SD of n=4 independent experiments, each performed on independent neuronal cultures for WT and A97S genotypes (20 images analyzed per condition in each experiment). hTTR WT Rac1i condition was tested only in 2 independent experiments as previous data showed no effect of the Rac1 inhibitor on hTTR WT neurons. *p < 0.00, ****p < 0.0001 by one-way ANOVA with Sidak's multiple comparisons test.

We followed by analyzing whether Rac1 inhibition could similarly ameliorate the axonal actin defects observed in mutant neurons. Indeed, Rac1 inhibition restored the decreased number of actin trails observed in hTTRA97S DRG axons (Figures 4F and 4G). The rescue of axonal actin defects was concomitant with a reversion of the decrease in synaptotagmin puncta in hTTRA97S neurons (Figures 4H and 4I), reinforcing the role of Rac1 as a key regulator of actin dynamics, which subsequently impacts the presynaptic vesicle network.

We then explored whether Rac1 could also be involved in the microtubule dysregulation observed in hTTRA97S peripheral axons. For that, we evaluated microtubule dynamics in DRG neuronal cultures from hTTRA97S-Thy1-EB3-GFP and hTTRWT-Thy1-EB3-GFP mice. Mutant neurons displayed an increased EB3 comet density in axon shafts, recapitulating the data obtained *ex vivo* in sural nerve axons (Figures 5A and 5B). Implying Rac1 involvement in the alterations of microtubule

dynamics, inhibition of the Rho GTPase reverted the increased EB3 comet density of hTTRA97S-Thy1-EB3-GFP DRG neurites (Figures 5A and 5B). These results suggest either that Rac1 dysregulation directly affects microtubule dynamics or that Rac1 inhibition, by rescuing actin defects, reverts microtubule alterations. Importantly, our data pinpoint Rac1 as a critical molecular player in the cytoskeletal alterations induced by mutant TTR.

Having demonstrated that Rac1 inhibition rescues cytoskeletal damage, a phenotype that precedes axonal degeneration in mutant neurons, we evaluated the potential of inhibiting Rac1 activity to prevent amyloidogenic TTR-induced axonal degeneration. We observed that Rac1 inhibition prevented neurodegeneration in DIV4 hTTRA97S neurons, as indicated by the restoration of the degeneration index of the mutant neurons (Figures 5C and 5D). These results show that blocking cytoskeleton alterations by inhibiting Rac1 in DRG neurons from an



Table 1. Study group demographic characteristics for genome-wide array genotyping					
	Males	Females	Range of AO	Mean AO	Standard deviation
Early onset	55	37	[21–39]	31.27	±4.31
Late onset	48	35	[50–90]	61.28	±8.36
Total	103	72	[21–90]	45.5	±16.38

ATTRv-PN mouse model prevents axonal degeneration, identifying Rac1 as a candidate therapeutic target for the disease.

A RACGAP1 variant is associated with disease onset in ATTRv-PN patients

The most prevalent pathogenic variant in ATTRv-PN is TTR Val30Met (ATTRV30M), and among carriers of this variant, there is significant diversity in phenotype, severity, and AO. To determine the relevance of Rac1 in human disease, we investigated whether variants in the genes encoding Rac1 and its activators, quanine nucleotide exchange factors (GEFs), and inactivators, Rac1 GTPase-activating proteins (GAPs), might be associated with variability of AO among ATTRV30M patients. We analyzed a total of 744 SNPs in RAC1, RAC1 GAPs, and RAC1 GEFs (Table S3). Our sample included a total of 175 patients with ATTRV30M amyloidosis belonging to 109 families, divided into two groups based on AO (Table 1). We found one SNP rs615382 in the RACGAP1 gene associated with a late disease onset (p < 0.001), specifically a mean increase of 20 years for heterozygous individuals and 34 years for homozygous individuals carrying the variant (Figure 6A). No SNPs in the other studied genes showed statistical significance (p > 0.05) when comparing early- and late-onset individuals. Bioinformatics analysis of this SNP was performed using Ensembl (www.ensembl.org, release 110) and HaploReg (https://pubs.broadinstitute.org/mammals/ haploreg/haploreg.php, HaploReg v4.2). The RACGAP1 gene encodes RacGAP1, a specific Rac1 GAP that inhibits the Rac1 GTPase activity. 13 The variant rs615382 is located in an intronic region of RACGAP1 and overlaps with an enhancer region.

Then, we analyzed the influence of SNP rs615382 on RACGAP1 expression. Plasmids encompassing the reference (C) and alternative (A) alleles of RACGAP1 rs615382 variant were transfected into two cell lines: HEK293T, a non-neuronal cell line, and SH-SY5Y, a cell line with neuronal-like characteristics. Subsequently, the activity of the luciferase gene reporter was quantified using a luminescence assay. The luciferase activity of RACGAP1 rs615382 A-allele showed a significant increase relative to RACGAP1 rs615382 C-allele, with a difference of approximately 35% and 20% in SH-SY5Y and HEK293T cells, respectively (Figures 6B and 6C). These results confirm that the alternative A-allele, which is associated with late-onset ATTRV30M amyloidosis, leads to higher RACGAP1 expression. This finding provides direct evidence that rs615382 plays a critical role in modulating the expression of RACGAP1, suggesting that increased RacGAP1 levels are linked to the later onset of the disease. To further confirm whether increased RACGAP1 expression is associated with late-onset ATTRv-PN, we performed qPCR in salivary gland biopsies from early- and late-onset patients. Human salivary gland biopsies have been successfully used as a tool for diagnosis

and research on ATTRv-PN. We detected increased RAGGAP1 levels in late-onset patients when compared to early-onset cases (Figure 6D), proposing that an increase in RacGAP1, which correlates with decreased Rac1 activity, is associated with a slower and less aggressive form of ATTRV-PN. To explore whether an inverse relationship between RacGAP1 and Rac1 activity is observed in the disease mouse model, we performed western blot analysis on sciatic nerve lysates from 9-month-old hTTRA97S mice, a time point during which Rac1 activity is increased. Racgap1 protein was detected in both control and mutant nerves, although differences were not statistically significant (Figure S5). These findings confirm that RacGAP1 is expressed in the mouse model and may contribute to Rac1 regulation; however, the regulatory context may differ from that in human patients carrying the RACGAP1 SNP. Future studies will be important to clarify the functional relationship between RACGAP1 expression and Rac1 activity in the context of ATTRv-PN.

DISCUSSION

The findings presented in this study demonstrate that Rac1 hyperactivation is a critical mediator of cytoskeletal dysfunction preceding axonal loss in ATTRv-PN. Moreover, we hypothesize that amyloidogenic TTR, through the interaction with RAGE, regulates Rac1 activity and that blocking TTR-induced activation of Rac1 prevents axonal degeneration.

Our analysis of actin alterations in hTTRA97S DRG neurons showed collapsed growth cones preceding axonal degeneration. Growth cone collapse is a well-known early feature of axonal degeneration, as seen in other models such as Friedreich's ataxia, an inherited ataxia characterized by degeneration of DRG neurons. We also found axonal actin defects, specifically a reduction in the number of actin trails, in hTTRA97S DRG neurites, fitting the pathologic scenario of ATTRv-PN where amyloidogenic TTR accumulates and contacts mature peripheral axons. This was a key finding, showing the role of axonal actin trails in maintaining axon health by regulating the synaptic vesicle recycling and the impact of their dysregulation on axonal degeneration.

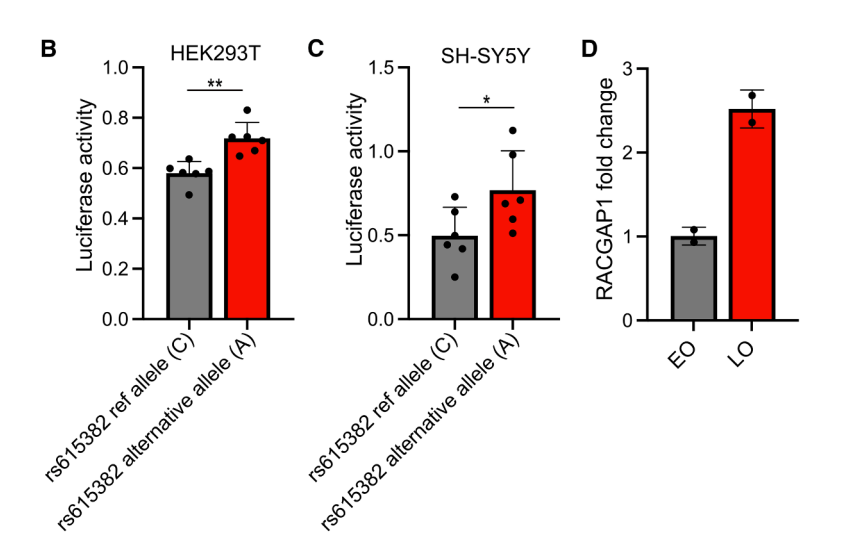
In addition to unraveling actin damage as a mediator of neurotoxicity in ATTRv-PN, our results substantiate an impairment in microtubule dynamics and axonal transport in hTTRA97S peripheral axons. Although we cannot disclose the primary defect induced by amyloidogenic TTR, our data suggest that a common pathway mediates the damage to actin and microtubules in ATTRv-PN, driven by Rac1. Mechanistically, an increase in Rac1 activity might contribute to the cytoskeleton defects observed in hTTRA97S axons. Rac1 is a well-established regulator of actin polymerization and branching, facilitating

CellPress OPEN ACCESS

Α

Statistical results of RACGAP1 SNP rs615382

Gene	dbSNP ID	В	Genotype	95% Wald Confidence Interval	P-value
	rs615382	-	CC (reference)	-	-
RACGAP1		19,99	CA	[13,41; 26,57]	<0,001
		34,08	AA	[25,35; 42,81]	<0,001



lamellipodia and filopodia formation through downstream effectors such as the WAVE complex and the Arp2/3 actin-nucleating complex.31 In the context of ATTRv-PN, Rac1 overactivity could lead to aberrant actin branching and disorganized filament networks, contributing to the growth cone collapse phenotype. Interestingly, in our proteomic analysis and in western blot analysis of DRG neuron cultures, we found Arpc1a and Arp3, two of the seven subunits of the human Arp2/3 protein complex, to be upregulated in hTTRA97S axons. Additionally, despite Rac1 being primarily recognized as an Arp2/3 activator, the Rho GTPase was shown to be able to both activate and inhibit Arp2/3-driven actin branching and polymerization, 32 which would also impact growth cone morphology. Our results also show that the reduction of actin trails in hTTRA97S DRG axons is mediated by the overactivity of Rac1. Actin trails were shown to be formin dependent and Arp2/3 independent in hippocampal neurons. 19 While we did not detect alterations in formins in our proteomic analysis, it is possible that an increase in Arp2/3, resulting in a limited G-actin pool, would inhibit formins, as few actin monomers would be available for polymerization. Additionally, Rac1 can regulate microtubule dynamics through pathways like PAK1 activation, which inactivates stathmin via phosphorylation, promoting microtubule polymerization.³³ Future work will be required to detail the molecular mechanism of Rac1 involvement in ATTRv-PN.

Importantly, we validated the relevance of Rac1 in human ATTRv-PN, since the variant rs615382 in the *RACGAP1* gene was significantly associated with delayed disease onset in

Figure 6. An SNP leading to the increased expression of RACGAP1, an inhibitor of Rac1 activity, is associated with late-onset ATTRV-PN

(A) Statistical results of *RACGAP1* SNP rs615382. B, unstandardized coefficient (estimated quantitative effect of each genotype on mean age-atonset variation, compared with the reference genotype); significance level was set to 0.05.

(B and C) Luciferase reporter gene assays for RACGAP1 rs615382 in HEK293T (B) and SHSY5Y cells (C). The activity of firefly luciferase was normalized to renilla luciferase activity and presented as a fold increase compared to the pGL3-promoter activity. Results presented as mean \pm SD of n=6 technical replicates.

(D) qPCR results for RAGGAP1 gene expression in salivary glands from early (EO) or late (LO) onset ATTRV30M patients. Data are shown as fold change in relation to EO samples. Data represent mean \pm SD of n=2 cases/disease onset.

*p < 0.05, **p < 0.01 by Student's t test. See also Figure S5.

ATTRV30M patients. The SNP identified was suggested to increase *RACGAP1* expression by disrupting the recombination signal binding protein for immunoglobulin kappa J region binding site to gene corepressors, such as silencing-mediator for retinoid/thyroid hormone re-

ceptor and Msx2-interacting nuclear target, 34-37 which would prevent the protein from repressing transcription.³⁸ Results from our reporter gene assays and qPCR data with salivary glands from ATTRv-PN patients substantiate this hypothesis, demonstrating that the alternative allele (A) of rs615382 indeed elevates RACGAP1 expression when compared to the reference allele (C). RacGAP1 has been studied primarily for its role in cell division and cytoskeletal dynamics, and our work underscores the importance of RacGAP1 in modulating neurodegenerative processes. Studies in zebrafish with a loss-of-function RACGAP1 mutation have demonstrated that RacGAP1 is required for the long-term survival of motor neurons and the cytoskeletal organization of sensory axons. 39 Also, the fact that we found the rs615382 SNP and increased RAGGAP1 expression associated with a later onset of ATTRV30M suggests that an increase in RacGAP1 might be translated to Rac1 inactivation leading to a lower rate of neurodegeneration.

Rac1 plays essential roles in many tissues, including the cardiovascular and immune systems, making targeted therapeutic interventions difficult without off-target effects. Although Rac1 inhibitors like NSC23766 have shown promise in our experimental model, their clinical use is challenging. Clinical trials of Rac1 inhibitors are still in the early stages, and achieving therapeutic specificity remains a significant hurdle. Nevertheless, our identification of the *RACGAP1* variant in ATTRv-PN patients, which enhances the expression of this Rac1 inactivator, offers a potential strategy to modulate Rac1 activity more selectively. We are currently working on AAV⁴⁰ and nanoparticle⁴¹ strategies





targeting the PNS to modulate *RACGAP1* in vivo. This approach represents significant progress from current treatments, which predominantly focus on TTR stabilization or gene silencing and do not address the downstream effects of TTR deposition on neuronal health.

In summary, we show that Rac1 inhibition preserves cytoskeletal integrity and prevents axonal degeneration in a mouse model for ATTRv-PN. Importantly, we establish that a variant in the gene encoding the Rac1-specific inactivator RacGAP1, which leads to its increased expression, is associated with a late-onset form of the disease. This work supports the neuroprotective effect of Rac1 inactivation in ATTRv-PN, offering new insights into the disease's molecular mechanism and identifying promising targets for therapeutic intervention. Future research will be required to translate these findings into pre-clinical studies, with the ultimate goal of improving outcomes for patients with ATTRv-PN.

Limitations of the study

This study identifies Rac1 hyperactivation as a driver of cytoskeletal disruption in ATTRv-PN and highlights RACGAP1 as a potential modulator of disease onset. However, the analysis of RACGAP1 expression was limited to a small number of patient samples, and future work should examine a broader cohort, including asymptomatic carriers, symptomatic individuals with both early- and late-onset disease, and unaffected controls. In addition, direct measurements of Rac1 activity in human tissue were not feasible, limiting our ability to confirm the functional link between RACGAP1 expression and Rac1 signaling in patients. Further studies in human-derived systems will be essential to validate the clinical relevance of this regulatory axis.

RESOURCE AVAILABILITY

Lead contact

Any additional information required to reanalyze the data reported in this paper is available from the lead contact, Márcia A Liz (mrliz@icbas.up.pt).

Materials availability

This study did not generate any new materials.

Data and code availability

- The mass spectrometry proteomics data have been deposited to the ProteomeXchange Consortium via the PRIDE partner repository with the dataset identifier PXD054291.
- No code was generated in this study.
- Any additional information required to reanalyze the data reported in this
 paper is available from the lead contact upon request.

ACKNOWLEDGMENTS

Thy1-EB3-GFP and Thy1-Mito-RFP mice were provided by Dr Thomas Misgeld (Technical University of Munich, Germany). We thank i3S Scientific Platforms (Animal Facility, Cell Culture and Genotyping, Histology and Electron Microscopy, Proteomics, Advanced Light Microscopy) (PPBIPOCI-01-0145-FEDER-022122) and the Glial Cell Biology Group at i3S, headed by João B. Relvas, for providing reagents for the FRET experiments. This work was supported by 2021 RD G- Transthyretin Amyloid Polyneuropathy (ATTR-PN) research competitive grant program from Pfizer to M.A.L.; FEDER - Fundo Europeu de Desenvolvimento Regional funds through the COMPETE 2020 – Operacional Programme for Competitiveness and Internationalisation (POCI), Portugal 2020, and by Portuguese funds through FCT - Fundação

para a Ciência e a Tecnologia/Ministério da Ciência, Tecnologia e Ensino Superior, in the framework of the project POCI-01-0145-FEDER-028336 (PTDC/MED-NEU/28336/2017) to M.A.L.; FCT 2022.01656.PTDC to C.L.; FCT IF/00902/2015 to M.A.L.; FCT to UMIB - Unit for Multidisciplinary Research in Biomedicine (UID/215/2025); FCT to ITR - Laboratory for Integrative and Translational Research in Population Health (LA/P/0064/2020 (DOI: 10.54499/LA/P/0064/2020); Ministry of Science and Technology, Taiwan Government (111-2320-B-002-079) to S.-T.H.; and National Taiwan University Hospital, Taipei, Taiwan (UN110-014) to S.-T.H. M.I.O.S. was supported by FCT 2023.08100.CEECIND, M.S. by FCT program D. 57/2016 - Norma Transitória, and J.P-d-F by FCT SFRH/BPD/113359/2015- program-contract described in paragraphs 4, 5, and 6 of art. 23 of law no. 1001 57/2016, of August 29, as amended by law no. 57/2017 of July 2019. FCT scholarship references: 2024.01389.BD to V.P.D. and UI/BD/154392/2023 to E.C.

AUTHOR CONTRIBUTIONS

J.M. and J.E., research concept, methodology, experimental work, data analysis, and writing original draft; V.P.D., methodology, experimental work, and proteomics analysis; G.N. and J.P.-d.-F., methodology, experimental work, and data analysis. M.I.O.d.S., M.M., A.D., E.C., and M.S., experimental work and data analysis. Y.Y.K., ATTR-PN mouse model generation; A.I.S., methodology; T.C. and R.T., provided human samples; C.L., research concept; S.-T.H., provided the ATTR-PN mouse model and research concept; and M.A.L., project design and supervision and manuscript editing and revision. All authors read and approved the final manuscript.

DECLARATION OF INTERESTS

The authors declare no competing interests.

STAR*METHODS

Detailed methods are provided in the online version of this paper and include the following:

- KEY RESOURCES TABLE
- EXPERIMENTAL MODEL AND STUDY PARTICIPANT DETAILS
 - o Subjects and study design
 - o Animals
 - o Cell lines
- METHOD DETAILS
 - o Myelinated axon quantification
 - o Quantification of skin innervation
 - o von Frey test
 - o TTR immunohistochemistry
 - Western blotting
 - o Proteomics
 - $\circ\,$ DRG primary cultures, plasmid expression, and drug treatment
 - O Validation of Rac1 silencing
 - $\,\circ\,$ Live imaging of DRG neurons
 - $\circ\,$ Live imaging of microtubule dynamics and axonal transport
 - o Immunocytochemistry
 - O Synaptotagmin-2 antibody uptake
 - o Imaging and quantification
 - o Rac1 pull down
 - DNA extraction and genome-wide array genotyping in ATTRv-PN patient samples
 - o Plasmid cloning of RACGAP1 variants
 - o Dual-luciferase reporter gene assays
 - o RNA isolation and real-time RT-PCR
- QUANTIFICATION AND STATISTICAL ANALYSIS

SUPPLEMENTAL INFORMATION

Supplemental information can be found online at https://doi.org/10.1016/j.celrep.2025.116411.

Cell Reports

Article

Received: February 13, 2025 Revised: May 5, 2025 Accepted: September 18, 2025

REFERENCES

- 1. Plante-Bordeneuve, V., and Said, G. (2011). Familial amyloid polyneuropathy. Lancet Neurol. 10, 1086-1097. https://doi.org/10.1016/S1474-4422 (11)70246-0.
- 2. Koike, H., Misu, K., Sugiura, M., Iijima, M., Mori, K., Yamamoto, M., Hattori, N., Mukai, E., Ando, Y., Ikeda, S., and Sobue, G. (2004). Pathology of early- vs late-onset TTR Met30 familial amyloid polyneuropathy. Neurology 63, 129-138. https://doi.org/10.1212/01.wnl.0000132966.
- 3. Koike, H., Ikeda, S., Takahashi, M., Kawagashira, Y., Iijima, M., Misumi, Y., Ando, Y., Ikeda, S.I., Katsuno, M., and Sobue, G. (2016). Schwann cell and endothelial cell damage in transthyretin familial amyloid polyneuropathy. Neurology 87, 2220-2229. https://doi.org/10.1212/WNL. 0000000000003362
- 4. Koike, H., Misu, K.i., Ikeda, S.i., Ando, Y., Nakazato, M., Ando, E., Yamamoto, M., Hattori, N., and Sobue, G.; Study Group for Hereditary Neuropathy in Japan (2002). Type I (transthyretin Met30) familial amyloid polyneuropathy in Japan: early- vs late-onset form. Arch. Neurol. 59, 1771-1776. https://doi.org/10.1001/archneur.59.11.1771.
- 5. Ikeda, S., Takei, Y., Yanagisawa, N., Matsunami, H., Hashikura, Y., Ikegami, T., and Kawasaki, S. (1997). Peripheral nerves regenerated in familial amyloid polyneuropathy after liver transplantation. Ann. Intern. Med. 127, 618-620. https://doi.org/10.7326/0003-4819-127-8_part_1-199710150-
- 6. Holmgren, G., Steen, L., Ekstedt, J., Groth, C.G., Ericzon, B.G., Eriksson, S., Andersen, O., Karlberg, I., Nordén, G., Nakazato, M., et al. (1991). Biochemical effect of liver transplantation in two Swedish patients with familial amyloidotic polyneuropathy (FAP-met30). Clin. Genet. 40, 242-246. https://doi.org/10.1111/j.1399-0004.1991.tb03085.x.
- 7. Coelho, T., Maia, L.F., Martins da Silva, A., Waddington Cruz, M., Planté-Bordeneuve, V., Lozeron, P., Suhr, O.B., Campistol, J.M., Conceição, I.M., Schmidt, H.H.J., et al. (2012). Tafamidis for transthyretin familial amyloid polyneuropathy: a randomized, controlled trial. Neurology 79, 785-792. https://doi.org/10.1212/WNL.0b013e3182661eb1.
- 8. Adams, D., Gonzalez-Duarte, A., O'Riordan, W.D., Yang, C.C., Ueda, M., Kristen, A.V., Tournev, I., Schmidt, H.H., Coelho, T., Berk, J.L., et al. (2018). Patisiran, an RNAi Therapeutic, for Hereditary Transthyretin Amyloidosis. N. Engl. J. Med. 379, 11-21. https://doi.org/10.1056/ NEJMoa1716153.
- 9. Benson, M.D., Waddington-Cruz, M., Berk, J.L., Polydefkis, M., Dyck, P.J., Wang, A.K., Planté-Bordeneuve, V., Barroso, F.A., Merlini, G., Obici, L., et al. (2018). Inotersen Treatment for Patients with Hereditary Transthyretin Amyloidosis. N. Engl. J. Med. 379, 22-31. https://doi.org/ 10.1056/NEJMoa1716793.
- 10. Maurer, M.S., Schwartz, J.H., Gundapaneni, B., Elliott, P.M., Merlini, G., Waddington-Cruz, M., Kristen, A.V., Grogan, M., Witteles, R., Damy, T., et al. (2018). Tafamidis Treatment for Patients with Transthyretin Amyloid Cardiomyopathy. N. Engl. J. Med. 379, 1007-1016. https://doi.org/10. 1056/NEJMoa1805689.
- 11. Eira, J., Silva, C.S., Sousa, M.M., and Liz, M.A. (2016). The cytoskeleton as a novel therapeutic target for old neurodegenerative disorders. Prog. Neurobiol. 141, 61-82. https://doi.org/10.1016/j.pneurobio.2016.04.007.
- 12. Kan, H.W., Chiang, H., Lin, W.M., Yu, I.S., Lin, S.W., and Hsieh, S.T. (2018). Sensory nerve degeneration in a mouse model mimicking early manifestations of familial amyloid polyneuropathy due to transthyretin Ala97Ser. Neuropathol. Appl. Neurobiol. 44, 673-686. https://doi.org/10.1111/nan. 12477.

- 13. Bagci, H., Sriskandarajah, N., Robert, A., Boulais, J., Elkholi, I.E., Tran, V., Lin, Z.Y., Thibault, M.P., Dubé, N., Faubert, D., et al. (2020). Mapping the proximity interaction network of the Rho-family GTPases reveals signalling pathways and regulatory mechanisms. Nat. Cell Biol. 22, 120-134. https:// doi.org/10.1038/s41556-019-0438-7.
- 14. Norgren, N., Olsson, M., Nyström, H., Ericzon, B.G., de Tayrac, M., Genin, E., Planté-Bordeneuve, V., and Suhr, O.B. (2014). Gene expression profile in hereditary transthyretin amyloidosis: differences in targeted and source organs. Amyloid 21, 113-119. https://doi.org/10.3109/ 13506129.2014.894908.
- 15. Sousa, M.M., do Amaral, J.B., Guimarães, A., and Saraiva, M.J. (2005). Upregulation of the extracellular matrix remodeling genes, biglycan, neutrophil gelatinase-associated lipocalin, and matrix metalloproteinase-9 in familial amyloid polyneuropathy. FASEB J. 19, 124-126. https://doi.org/10.1096/fj.
- 16. I Oliveira da Silva, M., Lopes, C.S., and Liz, M.A. (2020). Transthyretin interacts with actin regulators in a Drosophila model of familial amyloid polyneuropathy. Sci. Rep. 10, 13596. https://doi.org/10.1038/s41598-020-70377-4.
- 17. Njoo, C., Agarwal, N., Lutz, B., and Kuner, R. (2015). The Cannabinoid Receptor CB1 Interacts with the WAVE1 Complex and Plays a Role in Actin Dynamics and Structural Plasticity in Neurons. PLoS Biol. 13, e1002286. https://doi.org/10.1371/journal.pbio.1002286.
- 18. Munoz-Lasso, D.C., Molla, B., Calap-Quintana, P., Garcia-Gimenez, J.L., Pallardo, F.V., Palau, F., and Gonzalez-Cabo, P. (2020). Cofilin dysregulation alters actin turnover in frataxin-deficient neurons. Sci. Rep. 10, 5207. https://doi.org/10.1038/s41598-020-62050-7.
- 19. Ganguly, A., Tang, Y., Wang, L., Ladt, K., Loi, J., Dargent, B., Leterrier, C., and Roy, S. (2015). A dynamic formin-dependent deep F-actin network in axons. J. Cell Biol. 210, 401-417. https://doi.org/10.1083/jcb.201506110.
- 20. Burkel, B.M., von Dassow, G., and Bement, W.M. (2007). Versatile fluorescent probes for actin filaments based on the actin-binding domain of utrophin. Cell Motil Cytoskeleton 64, 822-832. https://doi.org/10.1002/ cm.20226.
- 21. Chenouard, N., Xuan, F., and Tsien, R.W. (2020). Synaptic vesicle traffic is supported by transient actin filaments and regulated by PKA and NO. Nat. Commun. 11, 5318. https://doi.org/10.1038/s41467-020-19120-1.
- 22. Pero, M.E., Meregalli, C., Qu, X., Shin, G.J.E., Kumar, A., Shorey, M., Rolls, M.M., Tanji, K., Brannagan, T.H., Alberti, P., et al. (2021). Pathogenic role of delta 2 tubulin in bortezomib-induced peripheral neuropathy. Proc. Natl. Acad. Sci. USA 118, e2012685118. https://doi.org/10.1073/ pnas.2012685118.
- 23. Almeida-Souza, L., Timmerman, V., and Janssens, S. (2011). Microtubule dynamics in the peripheral nervous system: A matter of balance. Bio-Architecture 1, 267–270. https://doi.org/10.4161/bioa.1.6.19198.
- 24. Kleele, T., Marinković, P., Williams, P.R., Stern, S., Weigand, E.E., Engerer, P., Naumann, R., Hartmann, J., Karl, R.M., Bradke, F., et al. (2014). An assay to image neuronal microtubule dynamics in mice. Nat. Commun. 5, 4827. https://doi.org/10.1038/ncomms5827.
- 25. Misgeld, T., Kerschensteiner, M., Bareyre, F.M., Burgess, R.W., and Lichtman, J.W. (2007). Imaging axonal transport of mitochondria in vivo. Nat. Methods 4, 559-561. https://doi.org/10.1038/nmeth1055.
- 26. Ouyang, M., Sun, J., Chien, S., and Wang, Y. (2008). Determination of hierarchical relationship of Src and Rac at subcellular locations with FRET biosensors. Proc. Natl. Acad. Sci. USA 105, 14353-14358. https:// doi.org/10.1073/pnas.0807537105.
- 27. Schmalbruch, H. (1986). Fiber composition of the rat sciatic nerve. Anat. Rec. 215, 71-81. https://doi.org/10.1002/ar.1092150111.
- 28. Sousa, M.M., Du Yan, S., Fernandes, R., Guimaraes, A., Stern, D., and Saraiva, M.J. (2001). Familial amyloid polyneuropathy: receptor for advanced glycation end products-dependent triggering of neuronal inflammatory and apoptotic pathways. J. Neurosci. 21, 7576-7586. https://doi.org/10.1523/JNEUROSCI.21-19-07576.2001.





- Huttunen, H.J., Fages, C., and Rauvala, H. (1999). Receptor for advanced glycation end products (RAGE)-mediated neurite outgrowth and activation of NF-kappaB require the cytoplasmic domain of the receptor but different downstream signaling pathways. J. Biol. Chem. 274, 19919–19924. https://doi.org/10.1074/jbc.274.28.19919.
- Hong, Y., Shen, C., Yin, Q., Sun, M., Ma, Y., and Liu, X. (2016). Effects of RAGE-Specific Inhibitor FPS-ZM1 on Amyloid-beta Metabolism and AGEs-Induced Inflammation and Oxidative Stress in Rat Hippocampus. Neurochem. Res. 41, 1192–1199. https://doi.org/10.1007/s11064-015-1814-8.
- Mullins, R.D., Heuser, J.A., and Pollard, T.D. (1998). The interaction of Arp2/3 complex with actin: nucleation, high affinity pointed end capping, and formation of branching networks of filaments. Proc. Natl. Acad. Sci. USA 95, 6181–6186. https://doi.org/10.1073/pnas.95.11.6181.
- Sayyad, W.A., Fabris, P., and Torre, V. (2016). The Role of Rac1 in the Growth Cone Dynamics and Force Generation of DRG Neurons. PLoS One 11, e0146842. https://doi.org/10.1371/journal.pone.0146842.
- Wittmann, T., Bokoch, G.M., and Waterman-Storer, C.M. (2004). Regulation of microtubule destabilizing activity of Op18/stathmin downstream of Rac1. J. Biol. Chem. 279, 6196–6203. https://doi.org/10.1074/jbc. M307261200
- Oswald, F., and Kovall, R.A. (2018). CSL-Associated Corepressor and Coactivator Complexes. Adv. Exp. Med. Biol. 1066, 279–295. https://doi.org/10.1007/978-3-319-89512-3_14.
- Tanigaki, K., and Honjo, T. (2010). Two opposing roles of RBP-J in Notch signaling. Curr. Top. Dev. Biol. 92, 231–252. https://doi.org/10.1016/ S0070-2153(10)92007-3.
- Dieguez-Hurtado, R., Kato, K., Giaimo, B.D., Nieminen-Kelha, M., Arf, H., Ferrante, F., Bartkuhn, M., Zimmermann, T., Bixel, M.G., Eilken, H.M., et al. (2019). Loss of the transcription factor RBPJ induces disease-promoting properties in brain pericytes. Nat. Commun. 10, 2817. https://doi.org/10.1038/s41467-019-10643-w.
- Diaz-Trelles, R., Scimia, M.C., Bushway, P., Tran, D., Monosov, A., Monosov, E., Peterson, K., Rentschler, S., Cabrales, P., Ruiz-Lozano, P., and Mercola, M. (2016). Notch-independent RBPJ controls angiogenesis in the adult heart. Nat. Commun. 7, 12088. https://doi.org/10.1038/ncomms12088.
- Kopan, R., and Ilagan, M.X.G. (2009). The canonical Notch signaling pathway: unfolding the activation mechanism. Cell 137, 216–233. https://doi.org/10.1016/j.cell.2009.03.045.
- Warga, R.M., Wicklund, A., Webster, S.E., and Kane, D.A. (2016). Progressive loss of RacGAP1/activity has sequential effects on cytokinesis and zebrafish development. Dev. Biol. 418, 307–322. https://doi.org/10.1016/j.ydbio.2016.06.021.
- Chan, K.Y., Jang, M.J., Yoo, B.B., Greenbaum, A., Ravi, N., Wu, W.L., Sánchez-Guardado, L., Lois, C., Mazmanian, S.K., Deverman, B.E., and Gradinaru, V. (2017). Engineered AAVs for efficient noninvasive gene

- delivery to the central and peripheral nervous systems. Nat. Neurosci. 20, 1172–1179. https://doi.org/10.1038/nn.4593.
- Lopes, C.D.F., Gonçalves, N.P., Gomes, C.P., Saraiva, M.J., and Pêgo, A.P. (2017). BDNF gene delivery mediated by neuron-targeted nanoparticles is neuroprotective in, peripheral nerve injury. Biomaterials 121, 83–96. https://doi.org/10.1016/j.biomaterials.2016.12.025.
- Itoh, R.E., Kurokawa, K., Ohba, Y., Yoshizaki, H., Mochizuki, N., and Matsuda, M. (2002). Activation of rac and cdc42 video imaged by fluorescent resonance energy transfer-based single-molecule probes in the membrane of living cells. Mol. Cell Biol. 22, 6582–6591. https://doi.org/ 10.1128/MCB.22.18.6582-6591.2002.
- Alves-Ferreira, M., Coelho, T., Santos, D., Sequeiros, J., Alonso, I., Sousa, A., and Lemos, C. (2018). A Trans-acting Factor May Modify Age at Onset in Familial Amyloid Polyneuropathy ATTRV30M in Portugal. Mol. Neurobiol. 55, 3676–3683. https://doi.org/10.1007/s12035-017-0593-4.
- 44. Breckwoldt, M.O., Pfister, F.M.J., Bradley, P.M., Marinković, P., Williams, P.R., Brill, M.S., Plomer, B., Schmalz, A., St Clair, D.K., Naumann, R., et al. (2014). Multiparametric optical analysis of mitochondrial redox signals during neuronal physiology and pathology in vivo. Nat. Med. 20, 555–560. https://doi.org/10.1038/nm.3520.
- Eira, J., Magalhães, J., Macedo, N., Pero, M.E., Misgeld, T., Sousa, M.M., Bartolini, F., and Liz, M.A. (2021). Transthyretin Promotes Axon Growth via Regulation of Microtubule Dynamics and Tubulin Acetylation. Front. Cell Dev. Biol. 9, 747699. https://doi.org/10.3389/fcell.2021.747699.
- Liz, M.A., Mar, F.M., Santos, T.E., Pimentel, H.I., Marques, A.M., Morgado, M.M., Vieira, S., Sousa, V.F., Pemble, H., Wittmann, T., et al. (2014). Neuronal deletion of GSK3beta increases microtubule speed in the growth cone and enhances axon regeneration via CRMP-2 and independently of MAP1B and CLASP2. BMC Biol. 12, 47. https://doi.org/10.1186/1741-7007-12-47.
- Sampathkumar, C., Wu, Y.-J., Vadhvani, M., Trimbuch, T., Eickholt, B., and Rosenmund, C. (2016). Loss of MeCP2 disrupts cell autonomous and autocrine BDNF signaling in mouse glutamatergic neurons. eLife 5, e19374. https://doi.org/10.7554/eLife.19374.
- Seixas, A.I., Morais, M.R.G., Brakebusch, C., and Relvas, J.B. (2023).
 A RhoA-mediated biomechanical response in Schwann cells modulates peripheral nerve myelination. Prog. Neurobiol. 227, 102481. https://doi. org/10.1016/j.pneurobio.2023.102481.
- Miller, S.A., Dykes, D.D., and Polesky, H.F. (1988). A simple salting out procedure for extracting DNA from human nucleated cells. Nucleic Acids Res. 16, 1215. https://doi.org/10.1093/nar/16.3.1215.
- Felicio, D., Dias, A., Martins, S., Carvalho, E., Lopes, A.M., Pinto, N., Lemos, C., Santos, M., and Alves-Ferreira, M. (2023). Non-coding variants in VAMP2 and SNAP25 affect gene expression: potential implications in migraine susceptibility. J. Headache Pain 24, 78. https://doi.org/10. 1186/s10194-023-01615-z.



STAR*METHODS

KEY RESOURCES TABLE

REAGENT or RESOURCE	SOURCE	IDENTIFIER
Antibodies		
Rabbit monoclonal anti-PGP9.5	Abcam	Cat# ab108986; RRID:AB_10891773
Custom-made rabbit anti-mouse TTR	This paper	N/A
Rabbit polyclonal anti-human TTR	DAKO	Cat# A0002; RRID:AB_2335696
Rabbit Polyclonal anti-Desmin	Abcam	Cat# ab8592 RRID:AB_306653
Mouse Monoclonal anti-Arp3	Santa Cruz Biotechnology	Cat# sc-48344; RRID:AB_626700
Rabbit Polyclonal anti-ERK1/2	Cell Signaling Technology	Cat# 9102; RRID:AB_330744
Rabbit monoclonal anti-Vinculin	Thermo Fisher	Cat# 700062; RRID:AB_2532280
Mouse monoclonal anti-Rac1	Abcam	Abcam Cat# ab33186; RRID:AB_777598
Mouse Monoclonal anti-RacGAP1	Santa Cruz Biotechnology	Cat# sc-271110; RRID:AB_10611939
Rabbit polyclonal anti-Synaptotagmin-2	Synaptic Systems	Cat# 105 222; RRID:AB_2619769
Mouse monoclonal anti-βIII tubulin	Promega	Cat# G7121; RRID:AB_430874
Goat Polyclonal anti-TrkA	R&D Systems	Cat# AF1056; RRID:AB_2283049
Goat Polyclonal anti-TrkB	R&D Systems	Cat# AF1494; RRID:AB_2155264
Goat Polyclonal anti-TrkC	R&D Systems	Cat# AF1404; RRID:AB_2155412
Donkey Anti-Mouse IgG (H + L) Antibody, Alexa Fluor 488 Conjugated	Invitrogen	Cat# A21202; RRID:AB_141607
Donkey anti-Rabbit IgG (H + L) Secondary Antibody, Alexa Fluor 568	Invitrogen	Cat# A10042; RRID:AB_2534017
Donkey anti-Mouse IgG (H + L) Secondary Antibody, Alexa Fluor TM 647	Invitrogen	Cat# A31571; RRID:AB_162542
Donkey anti-Rabbit IgG (H + L) Secondary Antibody, Alexa Fluor TM 488	Invitrogen	Cat# A21206; RRID:AB_2535792
Goat anti-Guinea Pig IgG (H + L) Secondary Antibody, Alexa Fluor TM 647	Invitrogen	Cat# A21450; RRID:AB_141882
Alexa Fluor® 488 AffiniPure® Donkey Anti-Goat IgG (H + L)	Jackson ImmunoResearch	Cat# 705-545-147; RRID:AB_2336933
Peroxidase AffiniPure [™] Goat Anti-Rabbit lgG (H + L)	Jackson ImmunoResearch	Cat# 111-035-003; RRID:AB_2313567
Peroxidase AffiniPure TM Goat Anti-Mouse lgG (H + L)	Jackson ImmunoResearch	Cat# 115-035-003; RRID:AB_10015289
Bacterial and virus strains		
Lentivirus f(syn)-SYP-GFP	Viral Core Facility Charité –Universitaetsmedizin Berlin	#BLV-177p
Biological samples		
Human salivary glands	Unidade Corino de Andrade at Centro Hospitalar Universitário de Santo António (UCA-CHUdSA)	N/A
Human blood samples	Unidade Corino de Andrade at Centro Hospitalar Universitário de Santo António (UCA-CHUdSA)	N/A
Chemicals, peptides, and recombinant protein	S	
Ammonium chloride (NH4Cl)	Merck	Cat# 1011450500
Bovine serum albumin (BSA)	Sigma	Cat# C1889
		(Continued on next pa

(Continued on next page)





Continued		
REAGENT or RESOURCE	SOURCE	IDENTIFIER
Collagenase-IV-S	Sigma	Cat# C1889
DMEM-F12 medium	PAN-Biotech	Cat# P04-41150
Epon	Electron Microscopy Sciences	Cat# 14120
Fetal bovine serum (FBS)	Sigma	Cat# F9665
Glutaraldehyde	Electron Microscopy Sciences	Cat# 16316
PureBlu TM DAPI Nuclear Staining Dye	Bio-Rad	Cat# 1351303
SDS	NZYTech	Cat# MB11601
Sodium cacodylate	Delta Microscopies	Cat# 12300
Triton X-100	Sigma	Cat# T9284
Uranyl Acetate	Electron Microscopy Sciences	Cat# 22400
Neuronal Growth Factor (NGF)	Alomone Labs	Cat# N-100
L-glutamine	Thermo Scientific	Cat# 25030024
B-27 TM Supplement	Gibco	Cat# 17504044
Osmium tetroxide	Electron Microscopy Sciences	Cat# 19190
Skim Milk Powder	Merck	Cat# 70166-500g
Immobilon Crescendo Western HRP substrate	Merck	Cat# WBLUR0500
Sodium chloride (NaCl)	Acros Organics	Cat# 207790010
Sodium orthovanadate	Sigma-Aldrich	Cat# S6508-10G
Rhodamine-conjugated Phalloidin	Thermo Scientific	Cat# R415
Protease Inhibitor Mix	Merck	Cat# GE80-6501-23
RIPA Buffer	Merck	Cat# R0278-50mL
Paraformaldehyde (PFA)	Delta Microscopies	Cat# GF750170-1010
Toluidin Blue	Sigma-Aldrich	Cat# 89640-5G
Laminin	Sigma-Aldrich	Cat# L2020
Penicillin/streptomycin	Gibco	Cat# 15140-122
Poly-L-lysine (PLL)	Sigma-Aldrich	Cat# P2636
NSC23766 (selective inhibitor of Rac1-GEF interaction)	Tocris Bioscience	Cat# 2161
5-Fluoro-2'-deoxyuridine (FluoU)	Sigma Aldrich	Cat# F0503
Neurobasal TM Medium, minus phenol red	Invitrogen	Cat# 12348-017
Sucrose	Merck	Cat# 1.07651.1000
Piperazine-1,4-bis(2-ethane-sulfonic acid) (PIPES)	Merck	Cat# 1.10220.0250
Egtazic acid (EGTA)	Sigma-Aldrich	Cat# E8145-10G
Magnesium chloride (MgCl ₂)	VWR	Cat# 1.05833.0250
Fish gelatin	Sigma-Aldrich	Cat# G7041-100g
Glutathione High Capacity Magnetic Agarose Beads	Merck	Cat# G0924-1ML
Ponceau S	Sigma-Aldrich	Cat# P3504-10G
PureBlu [™] DAPI Nuclear Staining Dye	Bio-Rad	Cat# 1351303
Osmium tetroxide	Electron Microscopy Sciences	Cat# 19190
Immobilon Crescendo Western HRP substrate	Merck	Cat# WBLUR0500
Halt TM Protease & Phosphatase Inhibitor Cocktail	Thermo Scientific	Cat# 78440
RIPA Buffer	Merck	Cat# R0278-50mL
Sucrose	Merck	Cat# 1.07651.1000

(Continued on next page)



Continued		
REAGENT or RESOURCE	SOURCE	IDENTIFIER
Glutathione High Capacity Magnetic Agarose Beads	Merck	Cat# G0924-1ML
D-(+)-Glucose	Sigma-Aldrich	Cat# G8270-1KG
N-2-hydroxyethylpiperazine-N-2- ethanesulfonic acid (HEPES)	Sigma-Aldrich	Cat# H4034-100g
Calcium chloride dihydrate (CaCl ₂ ·2H ₂ O)	Merck	Cat# 1.02382.1000
Magnesium sulfate heptahydrate (MgSO $_4$ ·7H $_2$ O)	Merck	Cat# 1.05886.0500
Sodium phosphate dibasic (Na2HPO4)	Sigma-Aldrich	Cat# S3264-500G
Potassium Chloride (KCI)	Merck	Cat# 1.04935.5000
Collagenase-IV-S	Sigma-Aldrich	Cat# C1889
Tween® 20	Sigma-Aldrich	Cat# P1379-500ML
FPS-ZM1 (High affinity antagonist of RAGE)	Merck	Cat# 553030
Normal Donkey Serum (NDS)	Sigma-Aldrich	Cat# D9663
DMEM, high glucose, GlutaMAX TM Supplement	Gibco	Cat# 10569010
Antibiotic-Antimycotic (100×)	Gibco	Cat# 15240062
TRIzol TM Reagent	Invitrogen	Cat# 15596026
DreamFect TM Gold	OZ Biosciences	Cat# DG80500
Critical commercial assays		
QIAamp® DNA Blood Mini Kit	QIAGEN	Cat# 1043368
Axiom TM Precision Medicine Diversity Array Kit	Thermo Scientific	Cat# 951962
Zymoclean Gel DNA Recovery Kit	Zymo Research	Cat# D4001
Q5® Site-Directed Mutagenesis Kit	New England Biolabs	Cat# E0554S
PureLink [™] RNA Micro Scale Kit	Invitrogen	Cat# 12183016
NZY First-Strand cDNA Synthesis Kit	NZYTech	Cat# MB12501
Deposited data		
Proteomics data	ProteomeXchange Consortium via the PRIDE	PXD054291
Experimental models: Cell lines		
HEK293T	ATCC	RRID:CVCL_0063
SH-SY5Y	The Leibniz Institute DSMZ	RRID:CVCL_0019
N1E-115	Merck Milipore	RRID:CVCL_0451
Experimental models: Organisms/strains		
nTTRwt/mTtrwt	Kan et al. ¹²	N/A
hTTRA97S/mTtrwt	Kan et al. ¹²	N/A
hTTRWT-Thy1-EB3-GFP	This paper	N/A
hTTRA97S-Thy1-EB3-GFP	This paper	N/A
hTTRWT-Thy1-MitoRFP	This paper	N/A
hTTRA97S-Thy1-MitoRFP	This paper	N/A
Oligonucleotides		
RacGAP1; sense primer: 5'-CGAAGTGCTCTGGATGTTA-3'	This paper	N/A
RacGAP1; antisense primer: 5'-TTGCTCCTCGCTTAGTTG-3'	This Paper	N/A
RacGAP1 rs615382; sense primer: 5'-CTCCCCTTCCcACAGCATAAT CACTAAACC-3'	This paper	N/A

(Continued on next page)





Continued			
REAGENT or RESOURCE	SOURCE	IDENTIFIER	
RacGAP1 rs615382; antisense primer: 5'-GAACCAGAGGTGATTC-3'	This paper	N/A	
Recombinant DNA			
pIRESneo3+GFP:UTR-CH	Matthieu Piel Lab, available from Addgene	Cat# 64359; RRID:Addgene_64359	
pRL-CMV Renilla Vector	Promega	Cat# E2261	
pGL3-promoter-RACGAP1-rs615382(C)	This paper	N/A	
pGL3-promoter-RACGAP1-rs615382(A)	This paper	N/A	
pRaichu-Rac1	Itoh, R.E. et al. ⁴²	N/A	
Software and algorithms			
Proteome Discoverer v.3.0.1.27	Thermo Fisher Scientific	RRID:SCR_014477	
Leica LAS X	Leica Microsystems	RRID:SCR_013673	
Fiji/ImageJ v.1.54g	NIH	RRID:SCR_002285	
GraphPad Prism v.8.0	GraphPad	RRID:SCR_002798	
lmageLab [™] v.6.0.1	Bio-Rad Laboratories	RRID:SCR_014210	
ClustVis	Tartu Ülikool	RRID:SCR_017133	
Axiom [™] Analysis Suite v.5.1	Applied Biosystems	N/A	
UniProt	The UniProt Consortium	RRID:SCR_002380	
PantherDB	University of Southern California	RRID:SCR_004869	
SPSS	IBM	RRID:SCR_002865	
Other			
CFX384 Touch Real-Time PCR Detection System	Bio-Rad	N/A	
Leica DMI6000 B	Leica Microsystems	RRID:SCR_018713	
Leica SP8 LIGHTNING confocal microscope	Leica Microsystems	RRID:SCR_01816	
Von Frey Hairs, Semmes-Weinstein set	Ugo Basile	Cat#: 37450-275	
Leica DM2000 LED	Leica Microsystems	RRID:SCR_020223	
Bioruptor® Plus Sonicator	Diagenode	Cat# B01020001	
Amersham Protran Premium 0.45 NC Western Blotting membranes	Amersham Biosciences	Cat# 10600013	
4D-Nucleofector TM System	Lonza	Cat# AAF-1002B	
Nikon ECLIPSE Ti	Nikon	RRID:SCR_021242	
Zeiss Axio Imager Z1 ApoTome	Zeiss	N/A	
FRET Analysis Fiji Macro	Advanced Light Microscopy, I3S PPBI-Portuguese Platform of Biolmaging	https://github.com/mafsousa/ 2DFRETratiometrics	

EXPERIMENTAL MODEL AND STUDY PARTICIPANT DETAILS

Subjects and study design

DNA samples from 175 ATTRv-PN ATTRV30M amyloidosis patients (Table 1) were collected at Corino de Andrade at Centro Hospitalar Universitário de Santo António (UCA-CHUdSA) and stored at Centro de Genética Preditiva e Preventiva (CGPP-IBMC, Porto) biobank, as authorized by the CNPD (National Commission for Data Protection). Salivary gland biopsies from ATTRV30M patients were also collected at UCA-CHUdSA. All patient samples were clinically characterized, and patients were observed by the same group of neurologists. Age-at-onset (AO) of each patient was also registered. According to the literature, the samples were divided according to AO into early-onset (EO), when symptoms appeared before the age of 50, and late-onset (LO) if symptoms appeared only after that age. ⁴³ The study was conducted on 92 DNA samples of EO patients, 83 DNA samples of LO patients, 2 salivary gland samples of EO patients, and 2 salivary gland samples of LO patients. Sex was recorded for all participants (Table 1), and analyses were adjusted for sex. The Ethics Committee of CHUdSA approved the study, and all participants gave their written informed consent.

Cell Reports

Article



Animals

Mice were handled according to European Union and National rules and all studies approved by the i3S Animal Welfare and Ethics Review Body and the Portuguese Veterinarian Board. All animals were maintained under a 12h light/dark cycle and fed with regular rodent chow and water ad libitum. Genotypes were determined from ear-extracted genomic DNA. 12 Human TTR knock-in mice, carrying either wild-type human TTR or A97S human TTR, were generated by replacing the mTtr gene with the hTTR gene without altering the promoter and enhancer sequences of mTtr, as previously reported. 12 Mice were maintained in a C57BL/6 background, and heterozygotes with the genotypes hTTRwt/mTtrwt (abbreviated as hTTRWT; controls) and hTTRA97S/mTtrwt (abbreviated as hTTRA97S) of both sexes were used in this study, as no sex-dependent phenotype differences were seen. For measuring microtubule dynamics and axonal transport, homozygous hTTRA97S/hTTRA97S and hTTRWT/hTTRWT mice were crossed with either Thy1: EB3-GFP²⁴ or Thy1-MitoRFP mice⁴⁴ (kindly provided by Dr Thomas Misgeld, Technical University of Munich, Germany), generating hTTRA97S-Thy1-EB3-GFP and hTTRWT-Thy1-EB3-GFP mice or hTTRA97S-Thy1-MitoRFP and hTTRWT-Thy1-MitoRFP mice, respectively.

Cell lines

The following cell lines were used in this study: N1E-115 cells (Sigma-Aldrich), an adrenergic cell line derived from the mouse neuroblastoma C1300 tumor; SH-SY5Y cells (DSMZ, Braunschweig, Germany), a human neuroblastoma derived cell line; and HEK293T cells (ATCC), a human embryonic kidney derived cell line. Cell lines used were commercially obtained and not independently authenticated. Mycoplasma contamination is routinely tested by our cell culture facility.

METHOD DETAILS

Myelinated axon quantification

Sural nerves from 9-month-old hTTRWT and hTTRA97S were collected and fixed overnight at 4°C with a solution of 2.5% glutaraldehyde and 2% paraformaldehyde (PFA) in 0.1 M sodium cacodylate buffer (pH 7.4), and post-fixed with 2% osmium tetroxide in 0.1 M sodium cacodylate buffer for 2 h at RT and stained with 1% uranyl acetate for 30 min. Samples were dehydrated and embedded in Epon (Electron Microscopy Sciences). Cross sections were cut at 500 nm using a diamond knife in an RMC Ultramicrotome (PowerTome, USA) and contrasted with toluidine blue. Image acquisition was performed with a brightfield microscope Leica DM2000 LED (Leica Microsystems, Germany) using a 40× objective. The total number of myelinated axons was determined in each cross-section, using the Cell Counter plugin from ImageJ, and normalized by the total nerve area.

Quantification of skin innervation

Mice were perfused with 2% Periodate-Lysine-Paraformaldehyde (PLP). The footpad tissues were postfixed with PLP for 2h and cryosectioned into 30μm free-floating sections perpendicular to the dermis. For immunohistochemistry, tissue sections were permeabilized with 0.3% Triton X-100 for 10 min, blocked with 10% BSA in 0.3% Triton in PBS for 1 h at RT, and incubated with rabbit anti-PGP9.5 (1:1,000; Abcam, ab108986) in blocking buffer overnight at 4°C. Incubation with anti-rabbit Alexa Fluor-conjugated secondary antibody was performed for 1 h at RT. Epidermal innervation was quantified following established protocols, and the slides were coded to ensure that measurements were blinded. 12 Any nerve fiber ascending from the subepidermal plexus with branches inside the epidermis was counted as one, while branches in the dermis were counted as separate fibers. ImageJ was used to measure the total length of the epidermis along the upper margin of the stratum corneum. Intraepidermal nerve fiber density was derived as the number of fibers per millimeter of epidermal length.

von Frey test

For von Frey hair testing, animals were acclimatized for 20 min in a chamber with a wire-mesh bottom allowing access to hind paws. For the test, retractable monofilaments (Aesthesio, Precise Tactile Sensory Evaluator, 37450-275) were used to apply a force to the mid-plantar surface of hind paws. Paw withdrawal or abrupt movement were considered positive responses. The withdrawal threshold equaled the weakest force to elicit paw withdrawal in 50% or more of the trials (n = 5 trials). The force of withdrawal is presented as the average value of the right and left hind paws.

TTR immunohistochemistry

Mice were perfused with PBS and sural nerves were collected and fixed with 4% PFA for 24 h. After cryoprotection in 30% sucrose, nerves were embedded in Optimum Cutting Temperature (OCT) compound (ThermoFisher Scientific) and cut longitudinally (Cryostat Leica CM3050S) in 10 μm thick sections. Slides were permeabilized with 0.5% Triton X-100 for 30 min at RT, guenched with 200 mM Ammonium Chloride for 30 min, and blocked with 5% normal donkey serum (NDS) in PBS for 1 h at RT. Incubation with rabbit anti-TTR (1:500, DAKO, A0002) was performed in blocking buffer overnight at 4°C. Incubation of Alexa Fluor-conjugated secondary antibody was performed for 1 h at RT in blocking buffer. Slides were incubated with DAPI (1:100, Bio-Rad, 1351303) for 10 min and mounted using FluoroMount-G mounting medium (Invitrogen, 00-4958-02).





Western blotting

9-month-old hTTRWT and hTTRA97S mice were perfused with PBS, and sural and sciatic nerves, and muscle collected. Tissue or DIV2 DRG neuron culture protein lysates were prepared in ice-cold RIPA lysis buffer (Merck, R0278), supplemented with a cocktail of protease inhibitors (Protease Inhibitor Mix, Merck, GE80-6501-23) and 1 mM sodium orthovanadate, and then sonicated in a water bath sonicator (Bioruptor Plus, Diagenode, Belgium). 5–10 μg (sural nerve), 15–20 μg (DRG and sciatic nerve) or 5μg muscle of protein extracts were separated under denaturing conditions in a 12% agarose gel, transferred to Amersham Protran Premium 0.45 μm nitrocellulose membranes (GE Healthcare Life Sciences), and blocked in 5% non-fat dried milk in TBS-T for 1 h at RT. Membranes were probed overnight at 4°C with primary antibodies: rabbit anti-human TTR (1:1,000; DAKO, A002); custom-made rabbit anti-mouse TTR antibody (1:500; produced against recombinant mouse TTR); rabbit anti-Desmin (1:1,000; abcam, ab8592); rabbit anti-mouse vinculin (1:3,000; Thermo Fisher, 42H89L44); mouse anti-Arp3 (1:500; Santa Cruz Biotechnology, sc-48344); rabbit anti-ERK1/2 (1:3,000; Cell Signaling, #9102); and mouse anti-RacGAP1 (1:500; Santa Cruz Biotechnology, sc-271110). Subsequently, incubation with the secondary antibodies anti-rabbit IgG-HRP (1:10,000; Jackson Research, 111-035-003) and anti-mouse IgG-HRP (1:10,000; Jackson Research, 115-035-003) was performed for 1 h at RT. Immunodetection was achieved by chemiluminescence using ECL (Millipore, WBLUR0500) and quantified using Image Lab software (version 6.0.1).

Proteomics

Proteomics was performed by the i3S Proteomics facility. For preparation of total protein extracts, sural nerves from 9-monthold hTTRWT and hTTRA97S were lysed in 100 µL ice-cold RIPA lysis buffer (TE buffer pH 8.0 (10 mM Tris and 1 mM EDTA), 140 mM NaCl (Acros Organics, 207790010), 0.1% SDS (stock 10%, NZYTech, MB11601), 1% Triton X-100 (Merck, T9284), supplemented with a cocktail of protease and phosphatase inhibitors (Halt Protease & Phosphatase Inhibitor Cocktail, Thermo Scientific, 78440). Samples were processed using the solid-phase-enhanced sample-preparation (SP3) method and enzymatically digested with Trypsin/LysC (2 μg) overnight at 37°C with agitation at 1,000 rpm. Peptide concentration within each sample was determined through fluorescence measurements. For protein identification and label-free quantification, a nanoLC-MS/MS setup was employed, which consisted of an Ultimate 3000 liquid chromatography system coupled with a Q-Exactive Hybrid Quadrupole-Orbitrap mass spectrometer (Thermo Scientific, Germany). The UniProt Mus Musculus Proteome Database (2022_05 version, 17132 entries) was used as a reference for protein identification. Proteomics data was analyzed using Proteome Discoverer software (version 3.0.1.27, Thermo Scientific, USA). To elucidate the distinct protein levels in control and hTTRA97S mutation groups, a series of data processing steps were applied to the raw data, including a minimum requirement of 2 unique or razor peptides, defining upregulated proteins based on abundance ratios (hTTRA97S/hTTRWT) of >1.50 and downregulated proteins with ratios of <0.67, setting a significance threshold for the abundance ratio ρ -value at <0.05 and determining that the protein needed to be detected in at least 2 samples within each experimental group for inclusion in the analysis. Protein functional enrichment analysis of the altered proteins in hTTRA97S versus hTTRWT sural nerves was performed with PANTHER 19.0 (http://pantherdb.org/). The online software tool ClustVis (https://biit.cs.ut.ee/clustvis/) was used to generate the heatmap. For this purpose, protein abundance ratio values were transformed using log2.

DRG primary cultures, plasmid expression, and drug treatment

For DRG neuron experiments, we confirmed that similar growth cone differences between genotypes were consistently present in DRG cultures derived from 1-, 3-, 6-, and 9-month-old mice (Figure S2C). Therefore, we used 4- to 8-week-old mice to maximize neuronal yield and viability while still reproducing the relevant phenotypes. Moreover, while most analyses were performed using DRGs collected from all spinal levels, we performed cultures with only L3–L5 DRGs to align with the sural nerve data. Primary cultures of DRG neurons (hTTRA97S and hTTRWT for all experiments except for *in vitro* EB3 dynamics in which hTTRA97S-Thy1-EB3-GFP and hTTRWT-Thy1-EB3-GFP were used) were performed as previously described. 45,46 DRG neurons were plated in 20 μ g/mL PLL +5 μ g/mL Laminin-coated glass surfaces in DMEM/F12 (Merck, D8437) supplemented with B27 (Gibco), 1% penicillin/streptomycin (Gibco), 2 mM L-glutamine (Gibco), and 50 ng/mL NGF (Millipore, 01–125)-DRG medium, at 37°C and 5% CO₂.

For growth cone morphology assessment and synaptotagmin quantification, neurons were plated at a density of 5,000 cells in 24-well plates and cultured for 24 h (DIV1) and 48 h (DIV2), respectively. For live imaging of actin trails, DRG neurons were transfected using the 4D Nucleofector Amaxa system (Lonza, Barcelona, Spain), with 0.5 μ g of pIRESneo3+GFP:UTR-CH (kindly provided by Dr Jorge Ferreira, i3S), expressing the calponin homology (CH) domain of utrophin (UTR) which binds specifically to F-actin, ¹⁹ plated at a density of 20,000 cells in coated 35 mm glass bottom μ -dishes (iBidi), and cultured for 48h. For live imaging of synaptophysin transport, DRG neurons, plated at a density of 15,000 cells in coated 35 mm glass bottom μ -dishes (iBidi), were transduced at DIV1 with the lentivirus f(syn)-pSyp-GFP-w (produced at the Viral Core Facility Charité – Universitaetsmedizin Berlin, BLV-177)⁴⁷ and imaged at DIV2. For assessment of transduction efficiency of synaptophysin-GFP, DRG neurons were plated at 5,000 cells in 24-well plates and transduced at DIV1 with the lentivirus f(syn)-pSyp-GFP-w. At DIV2, cells were fixed and imaged, and GFP fluorescence intensity was quantified to confirm comparable transgene expression levels between control and mutant neurons. For EB3 dynamics, hTTRA97S-Thy1-EB3-GFP and hTTRWT-Thy1-EB3-GFP neurons were plated at a density of 15,000 cells in coated 35 mm glass bottom μ -dishes (iBidi) and imaged at DIV2.



For FRET experiments, DRG neurons were transfected using the 4D Nucleofector Amaxa system with 1 μ g of Raichu Rac1 plasmid. ⁴² Cells were left in suspension for 24 h and were subsequently plated in a coated 4-well ibidi slide (iBidi) and cultured for an additional 24 h.

For experiments with Rac1 and RAGE inhibition, cells were plated in the presence of 50 μ M NSC23766 (Tocris Bioscience) and 10 μ M FPS-ZM1 (Merck Millipore), respectively. For transfection-mediated Rac1 silencing, DRG neurons were nucleofected with 0.75 μ g of the shRNA Rac1 (TRCN00000551888, Sigma-Aldrich) or shRNA scramble (Sigma-Aldrich) and 1.125 μ g of EGFP-C1 plasmid. After transfection, cells were left in suspension for 24 h and then plated in coated 24-well plates at a density of 5,000 cells and cultured for 24 h.

For degeneration index assessment, DRG neurons were plated in coated 24-well plates at a density of 10,000 cells in DRG medium and: i) DIV1 analysis: fixed 24 h after plating; ii) DIV2 analysis: plated with 60 μ M 5-Fluoro-2'-deoxyuridine (FluoU) and fixed 48 h later; iii) DIV4 analysis: plated with 60 μ M FluoU, refreshed with 60 μ M FluoU (and 50 μ M NSC23766, when testing Rac1 inhibition) at DIV2 and fixed at DIV4.

Validation of Rac1 silencing

N1E-115 cells (Sigma-Aldrich) were grown in DMEM supplemented with 2mM L-glutamine, 10% FBS, and 1% P/S in uncoated 24-well plates at a density of 150,000 cells/well. At DIV1, cells were transfected with 0.5 μ g of the shRNA Rac1 or shRNA scramble (Sigma-Aldrich) using lipofectamine 2000. At DIV3, protein extracts were prepared in lysis buffer (0.3% Triton X-100, 1× protease inhibitor Cocktail, and 1mM Sodium orthovanadate). 20 μ g of protein extracts were separated under denaturing conditions in a 12% agarose gel, transferred to Amersham Protran Premium 0.45 μ m nitrocellulose membranes (GE Healthcare Life Sciences), and blocked in 5% non-fat dried milk in TBS-T for 1 h at RT. Membranes were probed overnight at 4°C with primary antibody mouse anti-Rac1 (1:2,000; Abcam, ab33186) and subsequently with the secondary antibody anti-mouse IgG-HRP (1:10,000; Jackson Research, 115-035-003) in TBS-T for 1 h at RT. Immunodetection was performed by chemiluminescence using ECL (Millipore, WBLUR0500) and quantified using ImageJ software.

Live imaging of DRG neurons

Live imaging of actin trails on GFP:UTR-CH transfected neurons was performed in a Nikon Eclipse Ti (Nikon, Japan) inverted epifluor-escence microscope equipped with an IRIS 9 camera (Teledyne Photometrics, USA) with the following settings: PL APO LAMBDA 60×/1,4 Oil DIC WD 0.13 mm objective, 12% LED power and ND4 filter. Transfected neurites were identified based on morphology, and only neurons with unambiguous morphology were selected for imaging. GFP:UTR-CH was typically imaged at 1 frame/300 s for 2 min. To analyze GFP:UTR-CH kinetics, kymographs were performed using the Fiji KymoResliceWide plugin (distance-x axis; time-y axis). Actin trails appear in these kymographs as faint fluorescent lines, referred to as "fluorescent plumes". Starting and end positions of the traces and number of trails were defined using the Fiji Cell Counter.

Imaging of synaptophysin vesicles was conducted using a confocal Leica SP8 microscope (Leica Microsystems) and Leica Application Suite X (LAS X) software with a PL APO 63×/1.30 Glycerol objective. Image acquisition was performed over a 2 min period with frames captured at 2 s intervals. For quantification, the MTrackJ plugin from ImageJ was used and all parameters were assessed by manually tracking motile vesicles during 60 frames of each video.

For FRET, imaging was performed using a Leica DMI6000B inverted microscope. High-speed low-vibration external filter combinations (CFP excitation plus CFP emission [CFP channel], and CFP excitation plus YFP emission [FRET channel]) were mounted on the microscope (Fast Filter Wheels, Leica Microsystems). A 440-520nm dichroic mirror (CG1, Leica Microsystems) and an HCX PL APO 63×1.3NA glycerol immersion objective were used for CFP and FRET images. Images were acquired with 2Å~2 binning using a digital CMOS camera (ORCA-Flash4.0 V2, Hamamatsu Photonics). Shading illumination was online corrected for CFP and FRET channels using a shading correction routine implemented for the LAS AF software. CFP and FRET images were sequentially acquired using different filter combinations (CFP excitation plus CFP emission (CFP channel), and CFP excitation plus YFP emission (FRET channel), respectively). Ratiometric FRET was calculated as acceptor/donor, as described in. Image analysis was performed semi-automatically using an in-house developed macro for Fiji that allows for batch-processing of files (code available at https://github.com/mafsousa/2DFRETratiometrics). The main workflow consists of the following steps: 1) a preprocessing stage including shading correction and background subtraction (either by using a background image or by subtracting user-defined background mean intensity values); 2) cell segmentation using a user-selected channel, the best threshold algorithm and an option for user-dependent refinement; and 3) ratiometric analysis by dividing selected preprocessed channels in the segmented cell with final ratio images represented with a Royal LUT.

Live imaging of microtubule dynamics and axonal transport

To analyze microtubule dynamics and axonal transport in ex vivo live imaging, sural nerves were collected from hTTR (A97S or WT)-Thy1-EB3-GFP and hTTR (A97S or WT)-Thy1-MitoRFP mice, respectively, and placed in a 35 mm μ -Dish (iBidi) in pre-heated phenol-free Neurobasal medium (Thermo Fisher Scientific). To evaluate EB3 dynamics *in vitro*, DIV2 hTTRA97S-Thy1-EB3-GFP and hTTRWT-Thy1-EB3-GFP DRG neurons were imaged. Imaging of EB3 comets and mitochondria movement was conducted using a Leica SP8 microscope (Leica Microsystems) and Leica Application Suite X (LAS X) software with a PL APO $63 \times /1.30$ Glycerol objective. Image acquisition was performed for 2 min with frames captured every 2 s. For the quantification of EB3 dynamics,





kymographs were generated using the Fiji KymoResliceWide plugin (distance: x axis; time: y axis). The start and end positions of the kymograph slopes and the number of comets were defined using the Cell Counter plugin. Mitochondrial axonal transport was analyzed using the MTrackJ plugin from ImageJ and all parameters were assessed by manually tracking mitochondria during 30 frames of each video. To be considered, mitochondria needed to be tracked in at least 5 consecutive frames. The percentage of motile mitochondria was determined by tracking both motile and immobile mitochondria.

Immunocytochemistry

DRG neurons were fixed with cytoskeleton preservation fixative, PHEM (4% PFA, 4% sucrose, 0.25% Glutaraldehyde, 0.1% Triton X-100, 300 mM PIPES, 125 mM HEPES, 50 mM EGTA and 10 mM Magnesium Chloride), permeabilized with 0.2% Triton X-100 for 5 min, quenched with 200 mM Ammonium Chloride for 5 min and blocked with 2% Fetal Bovine Serum (FBS), 2% BSA and 0.2% Fish Gelatine in PBS for 1 h at RT. Incubation of primary antibodies was performed in 10% blocking buffer overnight at 4°C. The following antibodies were used: mouse anti-βIII-tubulin (1:2,000; Promega, G7121), rabbit anti-synaptotagmin-2 (1:500; SYSY, 105 222), goat anti-TrkA (1:250; R&D Systems, AF1494-SP); and goat anti-TrkC (1:250; R&D Systems, AF1404-SP). Alexa Fluor-conjugated secondary antibodies were incubated for 1 h at RT in 10% blocking buffer. Actin was labeled with the probe-conjugated dye Rhodamine-conjugated Phalloidin (1:100; Life Technologies, R415), in parallel with the secondary antibody.

Synaptotagmin-2 antibody uptake

DIV2 DRG cultures were initially incubated at RT for 10 min in Krebs-Ringer solution containing 128 mM NaCl, 25 mM HEPES, 4.8 mM KCl, 1.3 mM CaCl₂, 1.2 mM MgSO₄, 1.2 mM Na₂HPO₄, and 5.6 mM glucose (pH adjusted to 7.4). To induce exocytosis, the incubation buffer was replaced with a depolarizing solution in which KCl was increased to 55 mM and NaCl was reduced accordingly to maintain osmolarity. During the 5 min depolarization step at RT, cells were incubated with an antibody against the luminal domain of synaptotagmin-2 (1:50; SYSY, 105 222). Following incubation, cultures were rinsed three times with the original Krebs-Ringer buffer to remove unbound antibody. Cells were then fixed with PHEM for 30 min at RT. After fixation, cells were washed twice with PBS and permeabilized with 0.1% Triton X-100 in PBS for 5 min at RT. The samples were then blocked with 5% NDS for 1 h at RT and incubated with mouse anti-SNAP25 (1:1,000; BioLegend, 836304) in blocking buffer overnight at 4°C. Subsequent incubation with Alexa Fluor-conjugated secondary antibodies was performed for 1 h at RT. Image acquisition was performed as described in the corresponding sections.

Imaging and quantification

Immunocytochemistry images were acquired using an epifluorescence microscope Zeiss Axio Imager Z1 microscope with an Axiocam MR3.0 camera and Axiovision 4.7 software, using a Plan-Apo $63 \times 1.4A$ objective (growth cone analysis), an EC-Plan-Neofluar $40 \times /1.30$ Oil Ph3 objective (synaptotagmin imaging), a Plan-Apochromat $63 \times /1.40$ oil DIC (synaptotagmin antibody uptake) or an EC Plan Neofluar 20×0.50 NA objective (degeneration index).

Growth cones from DRG neurons labeled with ßIII-tubulin and phalloidin were qualitatively categorized according to their actin organization: the normal pattern containing the typical lamellipodia and filopodia structures, organized in a star-shaped morphology, and the collapsed pattern characterized especially by the absence of lamellipodia as well as growth cones with dystrophic actin morphologies, such as actin patches. Approximately 100 growth cones were analyzed in each condition using ImageJ software.

For synaptotagmin quantification, DRG neurites were randomly selected, and subsequent analysis was performed using Fiji software. A threshold was applied to the image and adjusted according to the fluorescent signal, allowing synaptotagmin particle analysis. Puncta number per neurite length was quantified by identifying puncta along at least 40 μ m of neurite per image.

For synaptotagmin recycling quantification, DRG neurites were randomly selected, and the analysis was performed using Fiji software. A threshold was applied to the SNAP25 image to define the presynaptic region. A second threshold was applied to the synaptotagmin image. The "Analyze Particles" tool was then used to quantify the number of synaptotagmin puncta that colocalized with the SNAP25-positive region. The number of synaptotagmin puncta was normalized to the measured neurite length, and results were expressed as synaptotagmin puncta density.

To assess axonal fragmentation through degeneration index quantification, the area occupied by the axons (total axonal area) and degenerating axons (fragmented axonal area) was analyzed using the particle analyser algorithm of ImageJ (size of small fragments = 20–10,000 pixels). The degeneration index was calculated as the ratio between fragmented and total axonal areas.

Rac1 pull down

Dissected sciatic nerves from hTTRWT and hTTRA97S mice were homogenized in lysis buffer (10% glycerol, 50 mM Tris-HCl pH 7.4, 100 mM NaCl, 1% NP-40, 2 mM MgCl2, and protease inhibitor cocktail [Sigma]). 10% of lysate volume was reserved to determine total protein amounts, and the remaining protein mixture was immunoprecipitated with the respective bait substrate (GST-tagged p21-activated kinase-binding domain [GST-PAK-PBD]), which was immobilized on Glutathione Sepharose beads (GE Healthcare). Bait-couple beads were incubated with lysates incubated with overnight at 4°C, washed with 10 packed volumes of lysis buffer, and bound proteins were eluted in GLB buffer (150 mM Trizma Base, 6% SDS, 0.05% Bromophenol



Blue, 30% glycerol, and 6 nM EDTA pH 8.8) with incubation at 95°C for 10 min. Samples were resolved on a 12% SDS PAGE gel, followed by standard Western blot and Ponceau *S* staining to confirm uniform pull-downs before detection with the relevant antibodies: mouse anti-Rac1 (1:500; Abcam, ab33186) and mouse anti-Vinculin (1:3,000; Thermo Fisher, 700062).

DNA extraction and genome-wide array genotyping in ATTRv-PN patient samples

Genomic DNA extraction from peripheral blood samples was performed using QIAamp DNA Blood Mini Kit.⁴⁹ DNA quantification was performed using Nanodrop One. The genotyping was attained with the Axiom Precision Medicine Diversity Array (PMDA, Affymetrix) and the GeneTitan Multi-Channel (MC) Instrument (Thermo Fisher Scientific, Waltham, MA, USA). Genotyping raw data was analyzed with the Axiom Analysis Suite version 5.1 (Applied Biosystems), using the Best Practices Workflow with default settings.

Data referring to single-nucleotide polymorphisms (SNPs) of the *RAC1* gene or its guanine nucleotide exchange factors (GEFs) and GTPase-activating proteins (GAPs) were exported and analyzed. The known RAC1-specific GAPs and GEFs are listed in Table S3.

Plasmid cloning of RACGAP1 variants

Plasmids were generated by inserting the genomic sequences (1186 base pairs in length) surrounding the *RACGAP1* rs615382 variant (NC_000012.11:g.50412911 C>A) into the pGL3-promoter vector (Promega, Fitchburg, WI, USA). This region of *RACGAP1* was amplified via PCR from the genomic DNA of an LO patient harboring the variant (rs615382 alternative allele A). The PCR product was then purified using the Zymoclean Gel DNA Recovery Kit (Zymo Research, Irvine, CA, USA) and subsequently cloned into the pGL3-promoter vector downstream of the firefly luciferase reporter gene by Gibson Assembly (New England Biolabs, Ipswich, MA, USA).

To obtain the reference allele configuration (rs615382 reference allele C), site-directed mutagenesis was performed using the Q5 Site-Directed Mutagenesis Kit (New England Biolabs, Ipswich, MA, USA), adhering to the protocol provided by the manufacturer, and the following primer pairs were used: forward primer 5'-CTCCCCTTCCcACAGCATAATCACTAAACC-3' and reverse primer 5'-GAACCAGAGGTGATTC-3'. Constructs sequences were confirmed by Sanger sequencing.

Dual-luciferase reporter gene assays

SH-SY5Y cells (DSMZ, Braunschweig, Germany) were cultured in a DMEM/F-12 high glucose GlutaMAX, supplemented with 10% fetal bovine serum (FBS) and 1% antibiotic-antimycotic solution (Gibco, Thermo Fisher Scientific, Waltham, MA, USA). HEK293T cells (ATCC) were cultured in DMEM high glucose GlutaMAX medium, also supplemented with 10% FBS and 1% antibiotic-antimycotic (Gibco, Thermo Fisher Scientific, Waltham, MA, USA). Dual-luciferase reporter gene assays were performed as described in. ⁵⁰ Briefly, for a period of 48 h, HEK293T and SH-SY5Y cells underwent transfection with vectors pGL3-promoter-RACGAP1-rs615382(C), pGL3-promoter-RACGAP1-rs615382(A), pGL3-control, or pGL3-promoter (150 ng per well) in 96-well white plates (CELLSTAR plates with μ Clear bottom; Greiner Bio-One, Kremsmünster, Austria). To monitor transfection efficiency, 15 ng of the internal control pRL-CMV renilla vector (Promega, Fitchburg, WI, USA) was co-transfected into cells. Transfection with the reagent DreamFect Gold (OZ Biosciences, Marseille, Provence-Alpes-Côte d'Azur, France) was performed following the manufacturer's guidelines. Complexes were added to each well with 100 μ L of medium devoid of antibiotic/antimycotic and either 1.5 \times 10⁴ cells/mL of HEK293T or 2.5 \times 10⁴ cells/mL of SH-SY5Y cells. After the 48 h transfection, the luciferase activity was quantified in the Synergy Mx Microplate Reader (Agilent, Santa Clara, CA, USA) by the Dual-Luciferase Reporter Assay System's protocol (Promega, Fitchburg, WI, USA).

RNA isolation and real-time RT-PCR

Total RNA was extracted from patient salivary gland tissues using the phenol-chloroform method with TRIzol reagent (Invitrogen, 15596026). The RNA was subsequently purified and isolated with the PureLink RNA Micro Kit (Invitrogen, #12183016), according to the manufacturer's instructions. An average of 1500 ng of total RNA was used to synthesize first-strand cDNA (NZY First-Strand cDNA Synthesis Kit, MB125). SYBR-green quantitative PCR (CFX384 Touch Real-Time PCR Detection System, Bio-Rad) was performed using specific primers. Human RACGAP1, sense primer: CGAAGTGCTCTGGATGTTA, antisense primer: TTGCTCCTCGCTTAGTTG; Human β -actin, sense primer: ACAGAGCCTCGCCTTTGCCG, antisense primer: CACCA TCACGCCCTGGTGC. The fold change in gene expression was calculated using the $\Delta\Delta$ Ct relative expression method (Livak method), and primers for β -actin were used as the endogenous control and calculated separately for each sample and respective condition.

QUANTIFICATION AND STATISTICAL ANALYSIS

All measurements were performed with the researcher blinded to the experimental condition. Data are shown as mean ± SD. Unpaired t-tests were used for comparing differences between two groups, while one-way ANOVA followed by Sisak's multiple comparisons was applied to identify significant differences among multiple groups. For the *in vivo* experiments, the sample size was chosen based on previous research.^{12,45} For the *in vitro* analysis, all the experiments were performed at least three times.





Statistical significance was determined using the GraphPad Prism Software version 8, being significance determined by $^*p < 0.05, ^{**}p < 0.01, ^{***}p < 0.001,$ and $^{****}p < 0.0001$. Statistical tests and sample sizes are indicated in each figure legend.

Regarding the genetic studies, since we included in the analysis several members of the same family, each patient was "nested" in his/her family. For this purpose, analyses were conducted taking into account the non-independence of age-at-onset (AO), using generalized estimating equations (GEEs). In this model, we associate the different variants with AO (which is the dependent variable), using the most common genotype as the reference and adjusting for sex. The unstandardized coefficient (B) corresponds to the mean AO variation observed in the individuals carrying a specific genotype when compared with the reference category. To correct for multiple testing, as we studied 9 genes, we applied a Bonferroni correction (α was set at 0.006 in the GEE analysis). Statistical analyses were performed using IBM SPSS Statistics software (v.29) (IBM, Armonk, NY, USA).